Applied Ocean Research 165 (2025) 104867

Contents lists available at ScienceDirect

Applied Ocean Research

journal homepage: www.elsevier.com/locate/apor

Research paper

Real-time open ocean wind waves from navigation radars for a truly global wind wave operational observing system

Elizaveta Ezhova [a,b], Natalia Tilinina [a], Sergey Gulev [a,c,*], Vitali Sharmar [a], Alexander Gavrikov [a], Boris Trofimov [d], Sergey Bargman [d], Peter Koltermann [e], Vika Grigorieva [a,f], Alexander Suslov [a]

[a] Shirshov Institute of Oceanology, RAS, Moscow, Russia
[b] Moscow Institute of Physics and Technology, Dolgoprudny, Russia
[c] University-Grenoble-Alpes, Grenoble, France
[d] JSC Marine Complexes & Systems LLC, St. Petersburg, Russia
[e] MSU, Moscow, Russia
[f] Tel Aviv University, Tel Aviv, Israel

ARTICLE INFO

Keywords:
Wind waves
Wave spectra
X-band radar
Ship observations
Global ocean monitoring systems

ABSTRACT

Global information about ocean wind waves is crucial for understanding their role in the climate system, validating model outputs, and assessing risks for shipping and marine structures. Recent advances in marine radar technologies have enabled accurate, high-resolution measurements of surface wind waves and their spectral characteristics. Making these measurements available in real-time opens a wide new range of products for many user communities. Here we introduce SeaVision, a ship-based monitoring system that, once integrated into a standard shipborne X-band radar, considerably improves real-time observational networks along major shipping routes. SeaVision automatically measures significant wave height, peak period and directional wave spectra at temporal resolutions down to seconds. First developed for research purposes in 2020, SeaVision passed an extensive period of validation using Spotter wave buoys and satellite data. Validation onboard research vessels was conducted for a wide range of latitudes, from the Arctic to Antarctica. SeaVision is fully operational, cost-effective, and capable of transmitting wave parameters continuously via satellite. Further developments of SeaVision allow for retrieving near surface wind speed, surface currents and ice parameters with the same resolution. Extensive installations of SeaVision (as well as similar systems) onboard commercial and research vessels allow for establishing a near-global observational network (as a part of GCOS and GOOS) largely exceeding capabilities of the present VOS network which over the last few decades are experiencing a dramatic decline and is also regionally complementing satellite missions. SeaVision will enhance coverage of the so far inadequately sampled global oceans.

1. Introduction

Reliable information about ocean surface waves is critically important for many scientific and practical needs. Being a key-component of the Earth System, wind waves serve as effective indicators of climate variability and change (Babanin et al., 2012; Cavaleri et al. 2012) and affect ocean-atmosphere energy and gas exchanges (Makin and Mastenbroek 1996; Gulev and Hasse 1998; Donelan et al. 2012; Mahrt et al. 2022; Wu et al. 2024 among others). Moreover, marine storminess has a profound impact on operations of marine carriers and naval architecture (Liu et al. 2024).

Nowadays, wind wave spectral models provide global and regional wind wave hindcasts with high spatial and temporal resolution (Jiang and Mu 2019; Echevarria et al. 2019; Jiang 2020; Sharmar et al. 2021; Aouf et al. 2021; Lobeto et al. 2022; Erikson et al. 2022 among others). These model products, however, require extensive validation against observations. At the same time, wind waves remain sparsely observed compared to the other ocean surface meteorological variables, such as sea surface temperature or sea level pressure. Despite their importance, achieving a sufficiently dense observational network for waves has

* Corresponding author at: Shirshov Institute of Oceanology, RAS, 36 Nakhimovsky ave., Moscow 117997, Russia.
E-mail address: gul@sail.msk.ru (S. Gulev).

https://doi.org/10.1016/j.apor.2025.104867
Received 6 September 2025; Received in revised form 8 November 2025; Accepted 17 November 2025
Available online 24 November 2025

always been challenging (Villas Boas et al. 2019).

Wind wave observations are available from several sources. Visual wave observations under the Voluntary Observing Ship (VOS) have the longest continuity (Gulev et al. 2003; Freeman et al. 2017; Liu et al. 2022) and were extensively used for the development of wind wave statistics at global and regional scales, as well as for the evaluation of long-term changes in wind seas and swells (Gulev and Grigorieva 2004, 2006) and the validation of satellite measurements (Grigorieva et al. 2022).

Satellite altimetry offers large-scale coverage of significant wave height (SWH), but with coarse temporal resolution and no direct spectral information (Liu et al. 2016; Dodet et al. 2020). The accuracy of remotely sensed wave characteristics strongly depends on the retrieval algorithms used. Satellite wave algorithms still have to be inter-compared to each other and calibrated against alternative information (Dodet et al. 2022). Synthetic Aperture Radar (SAR) missions such as CFOSAT and Sentinel-1 provide directional spectra, but their coverage is limited in both time and space, and retrievals depend heavily on empirical transfer functions (Collard et al., 2005). Developing a system capable of simultaneously monitoring wind, currents, and waves remains a challenge, even for advanced radar remote sensing. Wave buoys provide highly accurate in situ measurements, making them the primary validation source for remote sensing data and numerical models. However, they are extremely sparse, and their coverage remains mostly restricted to coastal regions and the tropical belt (Dodet et al. 2025).

In this respect shipborne radar technologies enabled the collection of accurate data of surface wind waves including their spectral characteristics. Since pioneering shipborne X-band radar-based wave measurements in the 1960s (Dremlyug 1961; Ijima and Takashi 1964) there has been impressive progress in the hardware and processing algorithms (see a detailed review by Huang et al. 2017). As a result, several commercial and scientific solutions were developed (see Table 1), which have proven to be effective and are deployed on some merchant and research vessels (Lund et al. 2012; Cornejo-Bueno et al. 2016; Chen et al. 2019; Derkani et al. 2021; Collins et al. 2025) as well as on coastal structures (Hessner and Hanson 2010). The primary limitation of the wide implementation of these systems is the need for onboard installation of an additional high-resolution radar, which greatly increases the cost of this technology. Recently developed coherent radar systems (Hwang et al. 2010; Carrasco et al. 2017; Ermoshkin et al. 2024) offer greater accuracy but are expensive and not used for routine navigation purposes. Moreover, all such systems rely on the short-pulse mode (Ziemer and Dittmer 1994; Dankert et al. 2005; Lund et al. 2014; Hessner et al. 2019), which provides the highest resolution (<10 m) but limits the operational range to 3 nautical miles – the mode used only in limited areas. Thus, adaptation of these systems for massive operations at different types of carriers remains a challenge; moreover, the very high cost of these systems is preventing their massive implementation.

Given the above-mentioned problems for the massive implementation of commercial radar systems, the dual use of the standard X-band navigation radars already installed on all SOLAS-compliant vessels for continuous wave monitoring becomes a challenge. Operating according to the IMO standards at the resolutions different from specialized commercial systems, they, however, provide global coverage along all shipping routes and may be considered as still underutilized platforms for routine ocean surface wave observations.

In this study we introduce SeaVision, a low-cost system that adds real-time wave monitoring functionality to existing navigation equipment (Tilinina et al. 2022). SeaVision connects via a splitter, operates without interfering with navigational functions, and delivers fully automated processing of radar signals to provide significant wave height, peak period, and directional wave spectra. Most importantly, it is designed for real-time transmission of wave data via the Global Telecommunication System (GTS) — a unique capability among existing ship-based radar systems.

The pilot version of the SeaVision system was first introduced by Tilinina et al. (2022). In this study, we present a completely new version for which the processing algorithm has been completely redesigned allowing for retrieving directional spectra of the wind wave field. Importantly, the algorithm is now built-into a modified hardware, allowing for an en-route real-time mode compatible with different operational settings of navigation radars. In Tilinina et al. (2022) the validation of SeaVision was limited to three cruises in the North Atlantic and Arctic onboard two vessels and for wave heights up to 4 m. We now performed validations using our new algorithm and extended the analysis to seven cruises, including those in the Southern Ocean and Central Atlantic waters, with wave heights reaching 8 m. This significantly broadens the range of environmental conditions under which the system has been tested, validated and to be used, including its performance in severe sea states.

The SeaVision system has been validated against Spotter buoy measurements and satellite altimetry on multiple cruises in diverse oceanic conditions, from the Arctic to the Southern Ocean. Its modular design and low cost enable scalable deployment across commercial and research vessels, addressing the critical gap in the in situ validation data for satellite missions and reanalysis products. As such, SeaVision has the potential to become a key component of the Global Ocean Observing System (GOOS) and Global Climate Observing System (GCOS).

Table 1
Existing marine X-band radar systems for sea state parameters measurements. Accuracy estimates are taken from the official technical documentation provided for each system or peer review publications.

Name	Need for additional radar installation	Additional sea parameters	Accuracy			Reference
			SWH (range)	Peak period (range)	Peak direction	
SeaVision IORAS, Russia	No	Surface currents, sea ice	0.5 m (0.7 – 18 m)	0.5 s (0 – 25 s)	10°	This study
WaMoS II Rutter Inc., Germany	Optionally Yes/No	Surface currents	0.5 m (0.7 – 18 m)	0.2 s (4 – 16 s)	2°	Reichert et al. 1999
Waves Miros AS, Norway	No	Surface currents	0.5 m (0.7 – 18 m)	0.5 s (3.2 – 5 s) 10 % (5 – 13 s) 20 % (13 – 25 s)	20°	www.miros-group.com
SeaDarQ Nortek Group, Norway	No	Oil spills, surface currents	N/A	N/A	N/A	Greenwood et al. 2018
WaveFinder Shindong Digitech, South Korea	N/A	N/A	0.5 m (0 – 3 m)10 % (3 – 20 m)	10 % (4 – 20 s)	10°	Shin et al. 2020
Hereon coherent-on-receive radar Helmholtz-Zentrum, Germany	No, modification of standard radar required	N/A	0.21 m	N/A	N/A	Horstmann et al. 2021

The paper is organized as follows. Section 2 presents the SeaVision architecture including the system design and signal processing algorithm. Section 3 presents results of the validation against wave buoys and satellite altimetry, including case studies. Section 4 compares SeaVision wave measurements with limited subsets of co-located visual VOS observations, thus underpinning Section 5 which discusses the potential of the SeaVision system for the global wind wave observing network. Conclusive Section 6 discusses the outlook and perspectives of further development.

2. System design and methods

2.1. SeaVision overview

SeaVision is a modular wave monitoring system composed of hardware and software components that extend the capabilities of standard marine X-band navigational radar without altering or interfering with its primary navigational function. It is designed as a compact digital processor that passively connects via a splitter to the radar output. Importantly, SeaVision does not replace the navigational radar or affect its display, which continues to serve ship safety and navigation needs. Instead, SeaVision adds an independent processing and display unit, offering real-time visualization of wave parameters, directional spectra, historical trends, and optional overlays such as ship positions via AIS and sea ice charts. Processed data are stored locally and can be transmitted in standard formats via GTS. Raw radar video can also be recorded for validation or other research applications.

2.2. SeaVision hardware design

Every marine carrier is equipped with non-coherent X-band radars with horizontal-horizontal polarization, as mandated by IMO standards. Navigational radars are designed to detect surrounding obstacles (ships, platforms, buoys, etc.) within dozens of kilometers, providing a 2D image of the surrounding sea surface. At the same time, the radar signal, modulated by ripples on the sea surface, inherently carries information about wind waves.

An X-band marine radar detects sea surface roughness via Bragg scattering, where centimeter-scale ripples modulate the return signal and reveal wind-driven gravity waves (Horstmann et al. 2015). In calm conditions, the sea surface acts as a mirror, but even light wind generate enough ripples for detection. The radar's spatial resolution L is given by

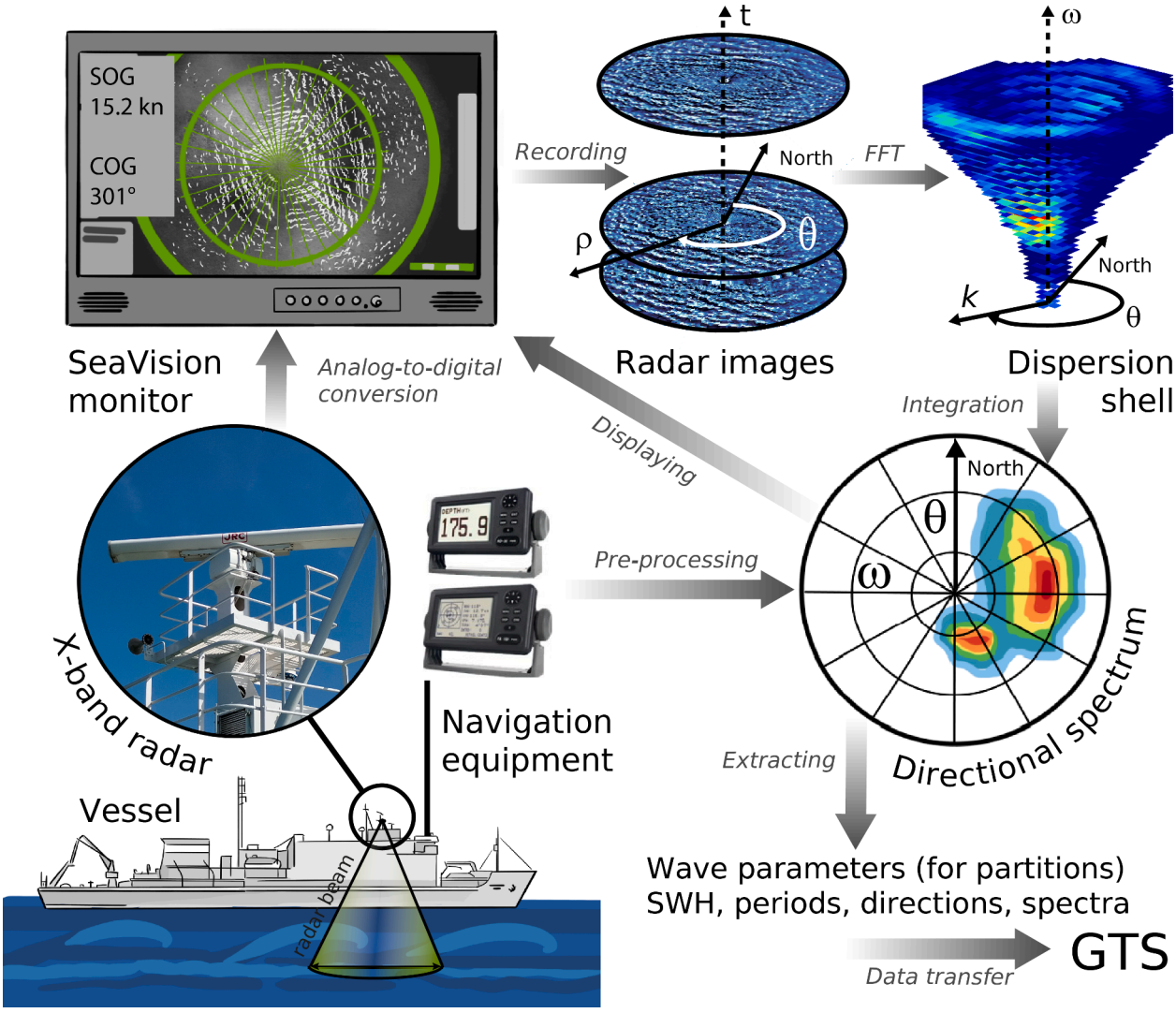

Fig. 1. Schematics of the operation of the SeaVision system. Signal from the sea surface (green) is digitized using an analog-to-digital converter and is converted into time series of radar images. The retrieval algorithm using Fast Fourier Transform (FFT) transposes these time series into a 3D spectrum, on which the dispersion shell is detected. Then it is converted into a directional wave spectrum. Final set of parameters, including SWH, periods and directions, directional spectrum $D(\omega, \theta)$ for given frequencies ω and directions θ, is transmitted through GTS.

$L = c \cdot \tau / 2$, where c is the speed of light and τ is the pulse duration. Standard systems achieve a 7–10 m resolution, with shorter pulses offering higher resolution at the cost of a reduced range to 3 nautical miles (~5.6 km), which is too close for normal navigation.

At the hardware level, the core of SeaVision is an analog-to-digital converter, developed in collaboration with "Marine Complexes and Systems LLC", which digitizes the analog radar output at 80 MHz. The data are extracted from the area with a 7.68 km radius around the vessel. As the radar antenna rotates, it transmits multiple signals along different azimuths. The beam width is typically ~1°, determining the angular resolution. Each scan along a single azimuth is digitized into 4096 radial cells with 8-bit resolution (0–255). One full antenna rotation (~2.5 s) yields a complete 4096 × 4096 matrix referred to as a snapshot. A time series of such snapshots forms the basis of the wave analysis. In addition to the radar signal, the system directly receives information from the vessel's navigation systems: speed and course relative to the ground, orientation, coordinates, and time. Using this data, the radar image is oriented to the north during the preprocessing stage. A general schematic of SeaVision operation is presented in Fig. 1. Information about SeaVision is added to Table 1 to be compared with the other commercial systems.

2.3. SeaVision wave parameters retrieval algorithm

Over the past four decades, numerous algorithms have been developed for extracting wave parameters from X-band marine radar, with significant advancements in both spectral analysis and image-based processing techniques (Huang et al., 2017). However, many of these approaches were tailored for high-frequency or coherent radar systems, often relying on high-resolution hardware and intensive computation. In contrast, SeaVision is designed to operate on non-coherent navigational radars with limited onboard resources, requiring to implement simple, robust, and computationally efficient methods. While modern developments in machine learning offer promising alternatives, especially for pattern recognition and adaptive filtering, these methods remain computationally demanding and less suitable for real-time operation on embedded systems. Therefore, we employ classical spectral methods that are not only well established but are also fast and lightweight in terms of memory use.

Our retrieval algorithm is based on the analysis of time series of radar snapshots collected during antenna rotation; processing details can be found in the Appendix. These snapshots are transformed into a three-dimensional wave number–frequency spectrum using a Fast Fourier Transform (FFT). From this spectrum, we extract the physical signal corresponding to the surface wave field by isolating the dispersion shell, which is identified using the linear dispersion relation for surface gravity waves following Young et al. (1985). Once the dispersion shell is determined, we compute the signal-to-noise ratio *SNR*, which represents the relative energy contained in the wave-consistent part of the spectrum. To convert this normalized spectral energy into physical units, we apply the Modulation Transfer Function (MTF) introduced by Nieto-Borge et al. (1999). Although we experimented with more complex MTF, including considering wind speed, humidity, wave age, these alternatives did not result in a significant improvement in retrieval accuracy under our operational constraints. Consequently, we adopted the classic MTF for its simplicity and proven reliability.

SeaVision is specifically designed to function in both stationary and underway modes, including at cruising speeds. The system has been tested on data collected while the vessel was moving at up to 17 knots. However, such speeds introduce additional complexity due to Doppler shifting. In the current implementation, we do not attempt to decompose the total Doppler term into its separate components, such as ship velocity, current speed, and others. Instead, we estimate the overall Doppler shift from the location of the dispersion shell on the frequency domain and apply a correction to convert the observed spectra into a stationary reference frame. While this approach does not yet allow estimating the surface current velocity at high vessel speeds (which is also measured with errors), it provides sufficient accuracy for the frequency spectrum correction. By knowing the speed of the vessel, we limit the estimate of the Doppler term from above.

Since the raw radar signal is not a direct measure of wave height, the estimation of significant wave height (SWH, H_s) requires calibration. We follow the approach proposed by Seemann et al. (1997) and later refined by Nieto-Borge et al. (2008), using a linear formula

$$H_s = A + B\sqrt{SNR}, \tag{1}$$

where A and B are calibration coefficients that depend on the specific radar model and its configuration, including antenna height, amplifier settings, and transmitter power. In contrast, wave direction, periods, and normalized spectra are available immediately after startup, as they do not require such tuning. Our experience shows that one month of SeaVision operation in the open ocean is generally sufficient to accumulate an adequate dataset of co-located points with altimeter tracks for calibration.

2.4. Limitations of SeaVision measurements

SeaVision, like any radar-based wave observing system, is subject to limitations associated with the impact of environmental conditions and with those associated with the system design. Environmental factors complicating radar image processing (equally for specialized commercial systems and SeaVision) include the presence of rain, sea ice, and nearby vessels within the scanning radius. Vessels appear as bright point targets on the radar display, interfering with the procedure of identification of contrast-enhanced sea-surface segments (part of the algorithm). This problem can be mitigated by cross-referencing Automatic Identification System (AIS) data to exclude overexposed sectors. Sea ice, while an obstacle for retrieving open-ocean wind wave characteristics, represents a valuable scientific signal itself. The radar imagery obtained during Antarctic cruises enables confident discrimination of sea ice with varying concentrations and structures, including broken ice. Recent advances in computer vision and machine learning methods now allow for the automatic generation of high-resolution ice maps from shipborne X- and S- band radars, the accuracies exceeding 90 % (Westbrook et al., 2025). Research of wave–ice interactions still remains limited, although X-band radar offers unique capabilities for analyzing wave behaviour in the presence of broken ice. Several studies (Collins et al. 2018; Kodaira et al. 2021) have demonstrated that ship-based observations can effectively capture wave propagation and attenuation in the marginal sea ice zone, including swell penetration and reduction of wave amplitude. Such observations are essential for calibrating and validating wave–ice interaction models and for improving forecasts of sea ice and wave conditions along maritime routes.

Rain also poses a limitation for X-band radar observations, as water droplets markedly scatter and attenuate the radar signal, obscuring the sea surface and hampering accurate retrievals. Recent studies propose effective algorithms for rain detection and mitigation based on texture analysis and deep learning models (Yang et al. 2021; Sun et al. 2022; Liu et al. 2023), and these approaches may be integrated into the SeaVision processing chain. However, our datasets contain <2 % of rainfall or snow episodes, suggesting that rain is not a dominant error source in our analysis.

The most important design-associated limitation of SeaVision is associated with the spatial resolution of standard navigation radars. While most scientific marine radar studies rely on the Short Pulse (SP) mode, achieving a range resolution below 10 m, operational bridge radars are typically used in Medium Pulse (MP) and Long Pulse (LP) modes, for which the effective resolution is an order of magnitude coarser. Fig. 2 illustrates how radar images change across SP, MP, and LP modes, using observations collected on 07:54—08:40 UTC 12 May 2024 near Cape Agulhas when SWH reached 4 m Validation experiments

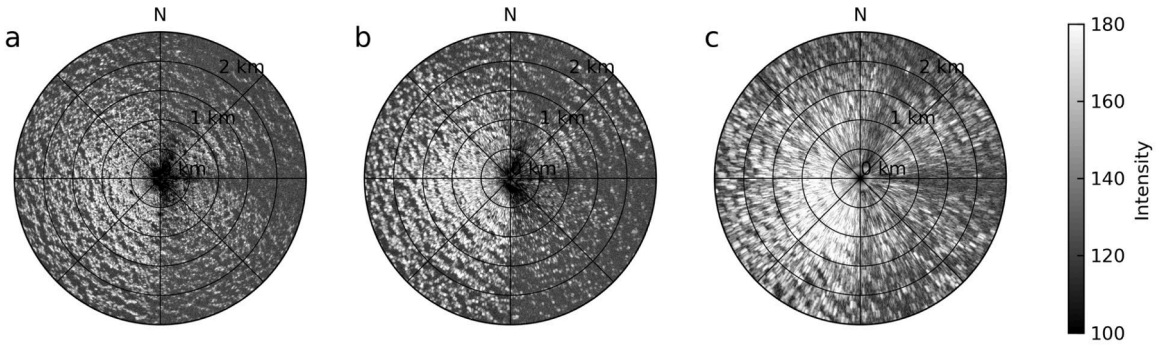

Fig. 2. Radar backscatter recorded by SeaVision within a radius of 2.5 km from the R/V *Akademik Fedorov* in units proportional to the intensity of the received signal, taken on 4 May 2024 in the Indian Ocean near Cape Agulhas. All images are oriented to the North. (a) SP mode with 8 m range resolution. (b) MP mode – 40 m (c) LP mode – 180 m.

during the AI65, AF50, and AF52 expeditions confirmed that SeaVision retrieval metrics degrade significantly in MP and LP modes. To improve SWH estimates under such conditions, we incorporated collocated wind speed data from onboard automatic weather stations (Airmar 220WX on R/V Akademik Ioffe and Milos 520 with WAA-151 anemometer on R/V Akademik Fedorov). For these cruises, significant wave height was retrieved using an empirical parameterization:

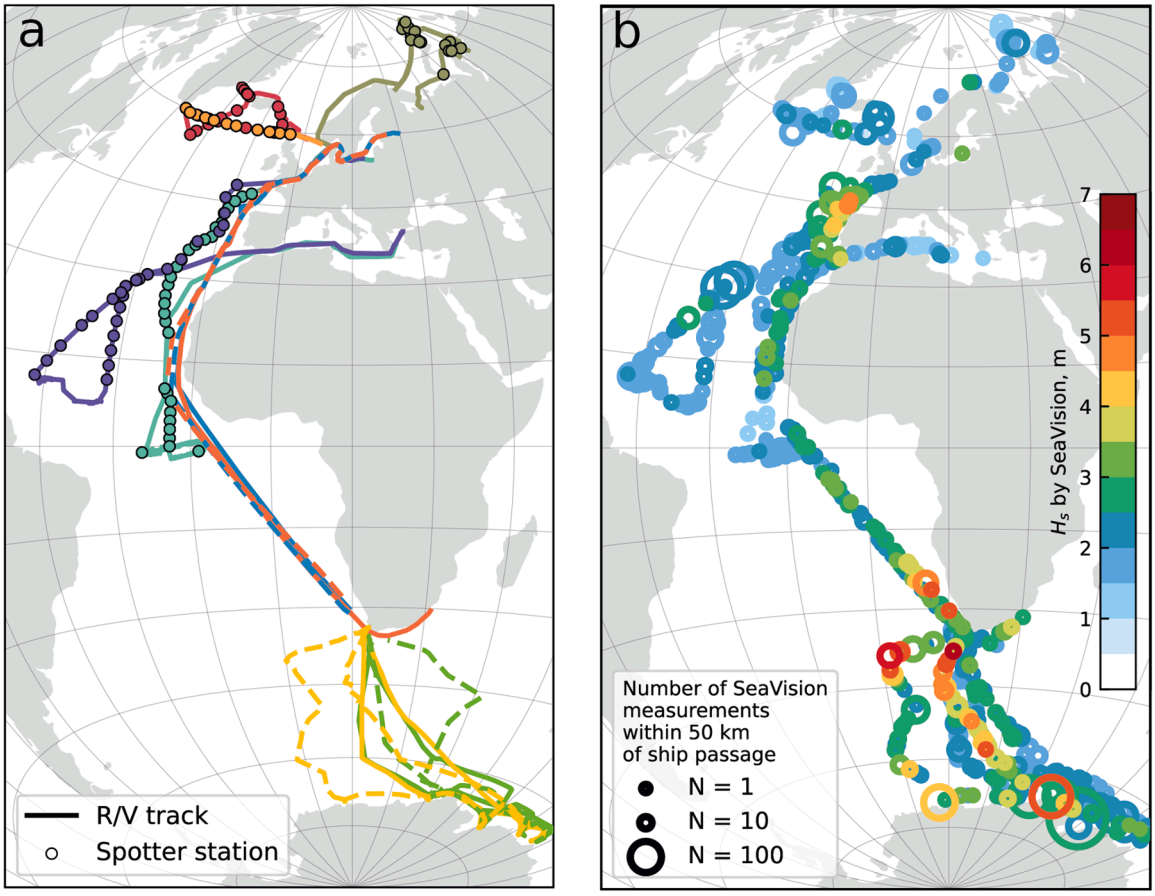

	ASV50	AI57	AI58	AI63	AI65	AF50/1 AF50/2 AF50/3 AF50/4	AF52/1 AF52/2 AF52/3 AF52/4
N_{buoy}	26 (96)	11 (97)	16 (127)	30 (197)	26 (657)		
N_{SV}	100 (376)	23 (119)	51 (368)	164 (377)	566 (1371)	600 (1893)	884 (1233)
N_{alti}	64 (279)	15 (101)	26 (186)	75 (239)	318 (962)	462 (1654)	311 (535)

Fig. 3. (a) Map of the research cruises of R/Vs *Akademik Sergey Vavilov* (ASV), *Akademik Ioffe* (AI), and *Akademik Fedorov* (AF) with Spotter buoy measurement stations (circles). Data of the AF50 and AF52 cruises of R/V *Akademik Fedorov* are divided into 4 stages. Legend shows the number of co-located stations with Spotter buoy N_{buoy}, with satellite altimeters in a 200 km circle of ship passage N_{alti}, total number of SeaVision measurements N_{SV} the number of 11-minute segments used for sampling. The number of measurement points after sampling is indicated in brackets. (b) SWH reconstructed from SeaVision data (color). Altogether panel (b) consists of 5537 single wave measurements, circles of different size show the number of single SeaVision measurements over 50 km ship passage.

$$H_s = A + B\sqrt{SNR}\cdot U, \quad (2)$$

where U is the true wind speed measured by the shipborne weather station. Thus, the use of SeaVision in combination with a weather station can significantly improve the results of determining SWH in MP and LP modes. In Section 3.3 we provide a comparative analysis of capabilities of SeaVision in different pulse modes. A detailed description of all algorithm procedures is provided in Appendix A.

3. Results

3.1. SeaVision data collection

During the period from 2020 to 2025 the SeaVision system was installed onboard of 3 research vessels (R/V) and used in different climate conditions in the Arctic, Atlantic and Southern Oceans (Fig. 3). Table 2 shows information about 7 cruises during which SeaVision was used and extensively calibrated. During the in-phase calibration period SeaVision was adopted to the three different navigation radar models (Table 2). Altogether collected SeaVision data amounted to 1000 h of observations providing 2900 individual measurements of the wave field. Calibration of SeaVision was performed using Sofar Spotter wave buoys (https://www.sofarocean.com/products/spotter). As many as 109 radar measurements were collocated with deploying a Spotter buoy in a drifting ship mode. Each drift measurement lasted between 30 min and 8 h. To expand the dataset, all stations were divided into 30-minute segments, resulting in a total of over 700 segments used for system calibration.

For the calibration at the drifting stations Sofar Spotter buoys were deployed on a 400-meter tether from the drifting R/V and each buoy recorded its own motion. These series were then processed using spectral analysis to obtain frequency wave spectra, SWH, peak and mean wave period, direction and directional spreading. Additionally, directional wave spectra from buoy data were reconstructed using the Extended Wavelet Directional Method (Peláez-Zapata et al. 2024).

3.2. Calibration of seavision against spotter buoy data

Fig. 4 demonstrates the results of the case study in the Bay of Biscay (48°N, 14°W) during 09:07—17:25 UTC 24 Dec 2023 when 4-meter waves were observed. The 8-hour time series was collected onboard R/V *Akademik Ioffe* (Fig. 4a). The R/V remained in a drifting mode within a one-kilometer radius, with the buoy being continuously trailing behind the stern (Fig. 4b). A moving 30-minute window with 10-minute intervals for averaging was used for data processing. The resulting 1D frequency and directional spectra for time period 12:30—13:00 UTC derived from the buoy data and SeaVision record demonstrate a close agreement with each other (Fig. 4c). Box-plots built for 1-hourly segments (Fig. 4d) show that differences between buoy and SeaVision records for SWH varied from few centimeters to a maximum of 20 cm. Bias in the peak period is typically within few tens of a second with a maximum of 0.6 s. Biases in mean periods and directions (Fig. 4d) are comparable to those identified for the peak values. The presence of two peaks in the spectrum complicates the analysis of T_p, so after 16 h the buoy began to register shorter period waves carrying more energy. Altimeter measurements from Sentinel-3B at 11:42 UTC within 80 km of the R/V and the buoy location also recorded 4-meter height waves (Fig. 4), supporting the validity of SeaVision measurements.

Another case study (Fig. 5) shows 30-minute time series of measurements in the central Atlantic (Fig. 5a). Fig. 5b shows that the distance between the buoy and the R/V changed over 30-minute time: the R/V tracker was mounted on the bow, while the buoy was deployed off the stern. Initially, they were about 150 m apart, but by the end of the time series, the distance increased to 450 m as the buoy slowly moved along the rope. Fig. 5c demonstrates high agreement between the retrieved wave spectra from Spotter and SeaVision, which both are peaking at 0.8 Hz and 1.3 Hz. The directional spectrum derived from SeaVision (Fig. 5c) shows even some greater details compared to the Spotter-derived spectrum. Box-plots (Fig. 5d) confirm a good agreement in SWH and mean direction estimates with <0.1 m bias in SWH and 4 degrees in direction. Mean periods (Fig. 5d) are also in a good agreement with the bias being smaller than 0.5 s.

The overall results of the validation of SeaVision are presented in Fig. 6 and Table 3. During calibration, the entire dataset was divided for training and testing in a proportion of 3:1 to make both samples sufficiently representative. We also tested a wide range of proportions (from 3:1 to 19:1) and the results were robust. The scatter plot built from all 1174 cross-validation measurements (Fig. 6a) demonstrates that in the range of <3 m wave height the averaged SWH bias between SeaVision and Spotter wave buoy is close to zero while for higher waves SeaVision tends to slightly underestimate the buoy wave height. The reason for this is likely associated with a shadowing effect, when the well-developed waves start to interact with each other affecting the radar signal propagating at grazing angles (Buckley et al. 1994, 1998). Radar systems may tend to underestimate the spectral energy at low frequencies and overestimate the energy at high frequencies (Borge et al. 2004; Magnusson et al. 2021). This requires a separate study, potentially involving the analysis of wind speed and wave age. The presence of multiple wave systems at a given location can lead to some discrepancies in the estimates of peak period and direction, both between instruments and across different temporal segments at the same station. Note that we also set a threshold of 70 cm on the minimum wave height since smaller

Table 2
Research cruises whose data are used in this work. The short names of the cruises correspond to the research vessels (R/V): ASV is *Akademik Sergey Vavilov*, AI is *Akademik Ioffe* and AF is *Akademik Fedorov*.

Short cruise name	Region	Distance sailed, km	Number of Spotter buoy measurements (number of 30-min segments)	Number of collocations with altimeter	Number of SeaVision measurements	Total time of measurements, hours	Radar model
ASV50	North Atlantic	10,465	26 (96)	279	376	528	JRC JMA–9110–6XA
AI57	North Atlantic	7745	11 (97)	101	119		JRC JMA–9122–6XA
AI58	Arctic	10,611	16 (127)	186	368		
AI63	Tropical Atlantic	20,792	30 (197)	239	177		
AI65	Tropical Atlantic	19,076	26 (657)	962	1371		
AF50	Atlantic, Antarctic	65,508	0	1654	1893	443	Sperry Marine BridgeDeck E 250
AF52	Atlantic, Antarctic	68,518	0	535	1233	377	
TOTAL		148,361	109 (1174)	3956	5537	1348	

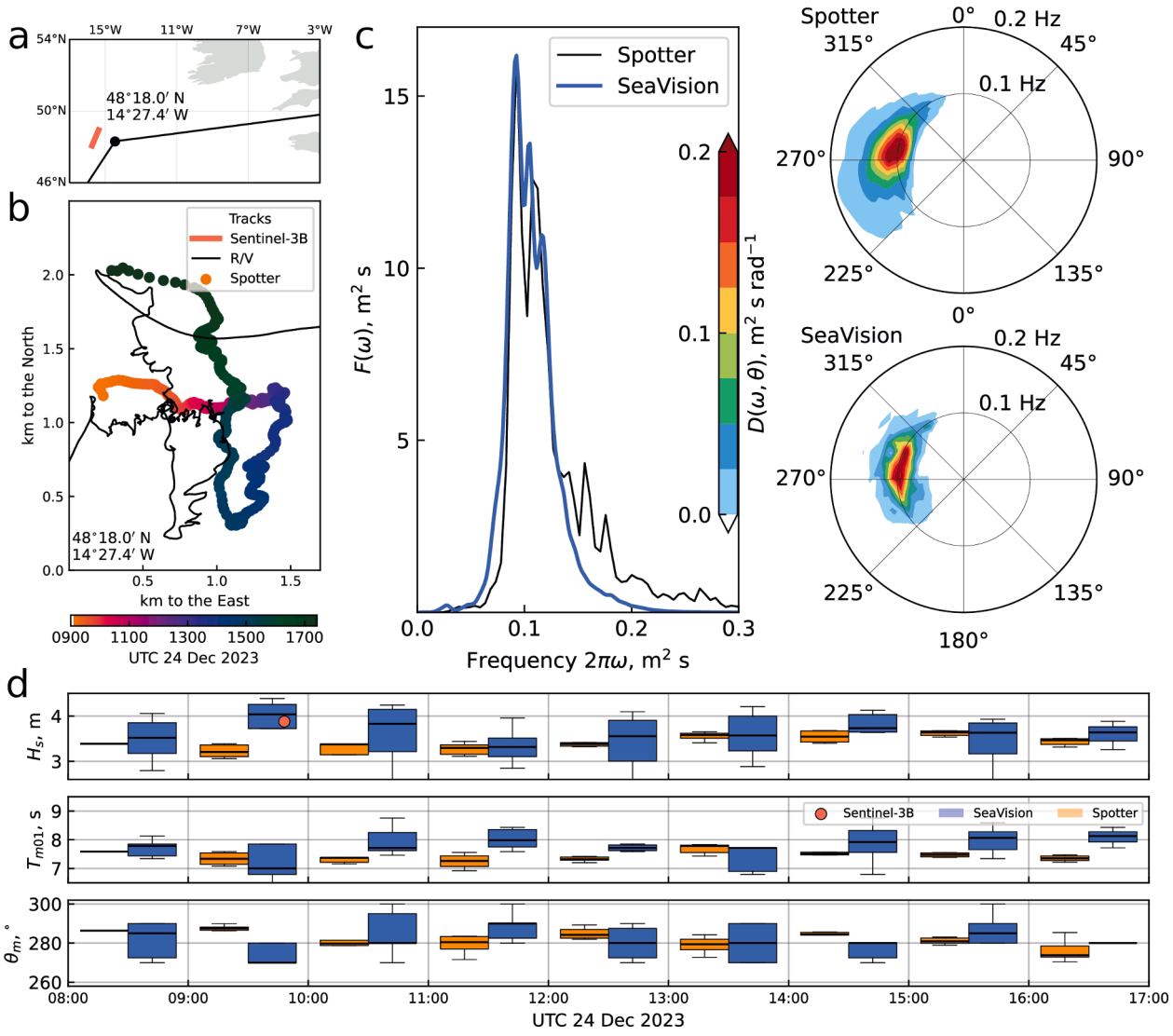

Fig. 4. Validation case study in the Bay of Biscay (48°N, 14°W; 09:07—17:25 UTC 24 Dec 2023): (a) Location of the station (black dot) and the R/V route (black line) with the segment of track of the satellite altimeter (Sentinel-3B). (b) Zoom on the region of the station measurements, showing the R/V track (black line) and the Spotter track (colour). (c) Reconstructed frequency spectra $F(\omega)$ derived from the Spotter buoy (black) and SeaVision (blue) and reconstructed directional spectra $D(\omega, \theta)$. (d) Box-plots of the 1-hourly segments of wave parameters (SWH H_s, mean period T_{m01} and direction θ_m) estimated from Spotter (yellow) and SeaVision (blue) data with altimetry data for SWH (red dot).

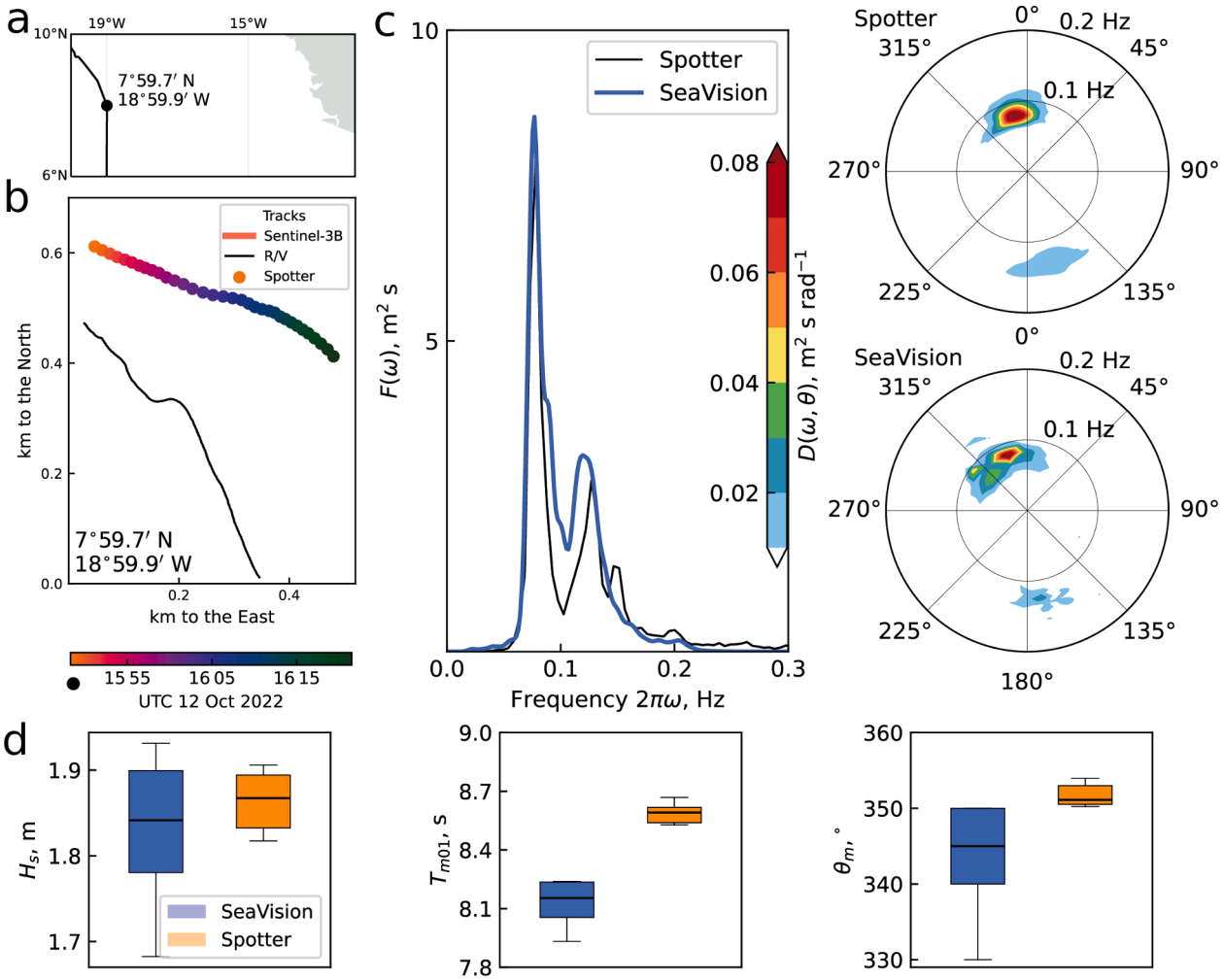

Fig. 5. Validation case study in the Central Atlantic (8°N, 19°W; 15:48—16:21 UTC 12 Oct 2022): (a) Location of the station (black dot) along the R/V route (black line). (b) Zoom on the region of the station measurements, showing the R/V track (black line) and the Spotter track (color). (c) Reconstructed frequency spectrum $F(\omega)$ derived from Spotter (black) and SeaVision (blue) data and reconstructed directional spectra $D(\omega, \theta)$ (d) Box-plot of SWH H_s, mean period T_{m01} and direction θ_m estimated from Spotter (yellow) and SeaVision (blue) data.

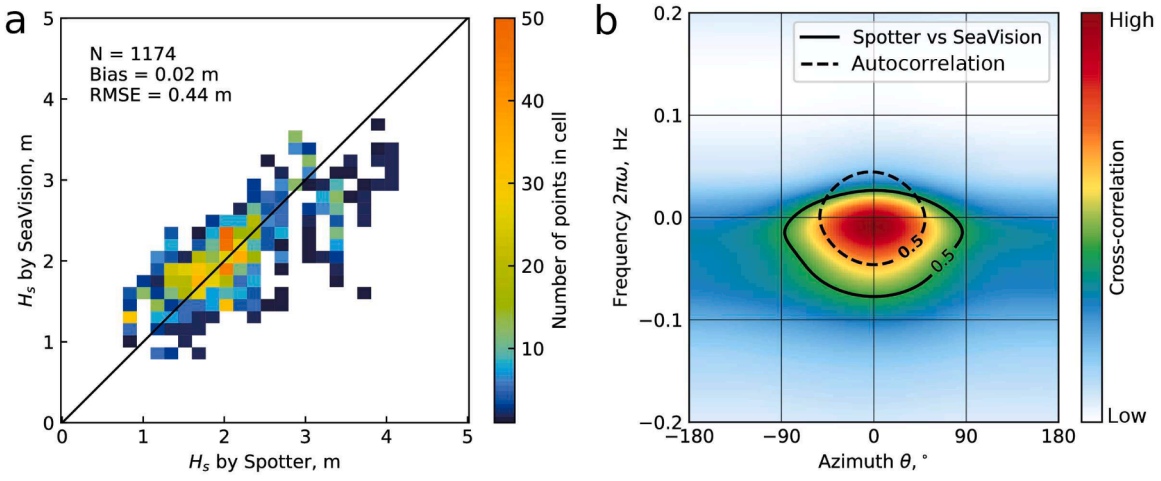

Fig. 6. (a) Scatter plot of SWH measured by buoy and retrieved by SeaVision algorithm for waves exceeding 70 cm, N is the number of validation segments. (b) Cross-correlation between directional spectra reconstructed from SeaVision and Spotter, averaged over the entire validation dataset. The contour line represents the threshold equal to half the maximum of the cross-correlation between the SeaVision system and the buoy (solid) and the autocorrelation of the buoy (dashed).

Table 3
Statistics of the validation of SeaVision algorithm against Spotter buoy data, parameter definitions are in the Appendix.

	H_s, m	T_p, s	T_{m01}, s	θ_p, °	θ_m, °	σ_p, °	σ_m, °
Bias	0.02	−0.1	−0.1	0	−0	−10	8
RMSE	0.44	0.5	0.4	10	7	18	11

waves were not resolved by the SeaVision at all. Limitation placed on the minimum wave height follows from surface roughness requirements. It can be shown that wind speeds of 3–5 m s^{-1} give a threshold for obtaining high-quality data (Ezhova et al. 2023).

Statistical comparison metrics (Table 3) imply the Root Mean Square error (RMSE) being about 0.44 m of the mean values for SWH and 0.5 s for the peak period. Comparisons performed for the mean periods and directions (also shown in Table 3) report very similar biases and RMSE to those derived for the peak values. These discrepancies are similar to those observed in analogous systems (Table 1) and are inherent into the method itself (Al-Habashneh et al. 2018), resulting from a minimum resolution of approximately 10 m, a temporal resolution of 2.5 s, and the use of incoherent radars. These limitations can be reduced by applying an advanced MTF (Nieto-Borge et al. 2004, Chen et al. 2015, Chernyshov et al. 2018) and accounting for the vessel motion (Chen et al. 2019), wind speed and direction. However, this would require significant computational resources and additional equipment, such as an inertial measurement unit and a weather station.

Analysis of our case studies above demonstrate the high consistency of directional wave spectra derived from SeaVision and buoy measurements. To evaluate the consistency between normalized directional spectra from buoys $D_b(\omega, \theta)$ and SeaVision $D_{SV}(\omega, \theta)$ we computed their cross-correlation across all co-located records. Fig. 6b shows that peak spectral energy exhibits no systematic bias in direction but is slightly shifted towards lower frequencies, indicating an overestimation of wave periods by the navigation radar. This shift likely arises because the system operates at the limit of spatial resolution. Radar systems are less capable of detecting short-period wind waves that do not satisfy the Nyquist criterion compared to the detection of relatively long waves. As a result, the cross-correlation pattern exhibits an asymmetry along the frequency axis. There is also a small scatter in the directional energy distribution. This is probably due to the high degree of dependence of radar image anisotropy on wind speed (Lund et al. 2012; Lund et al. 2014), which is not present in the buoy data.

3.3. SeaVision operation in "along the route" mode

The results of the validation against buoy data allows for considering extensive measurements in operational real-time mode when the SeaVision package inherently provides underway wind wave monitoring without interfering with any navigational tasks on the bridge. In contrast to timeseries obtained from one point, wave parameters measured along-the-way using radar should be less affected by sampling variability (Bitner-Gregersenet al. 2020).

The use of SeaVision in recording mode along the ship route was conducted during all cruises (Table 2) between the buoy stations. Collected raw data amount to about 23 GB for each 1-hourly segment, but automatically post-processed data are reduced to <2 MB for the storage strategy of every 10 min. During the cruises of R/V *Akademik Fedorov* in 2024 and 2025, the SeaVision system was configured as fully autonomous. Observations were conducted during the north-south Atlantic meridional transect and in the Southern Ocean, where alternative wave measurements are extremely sparse (Gulev et al. 2007; Babanin et al. 2019).

Fig. 7 presents a 36-hour record of a storm event off the coast of East

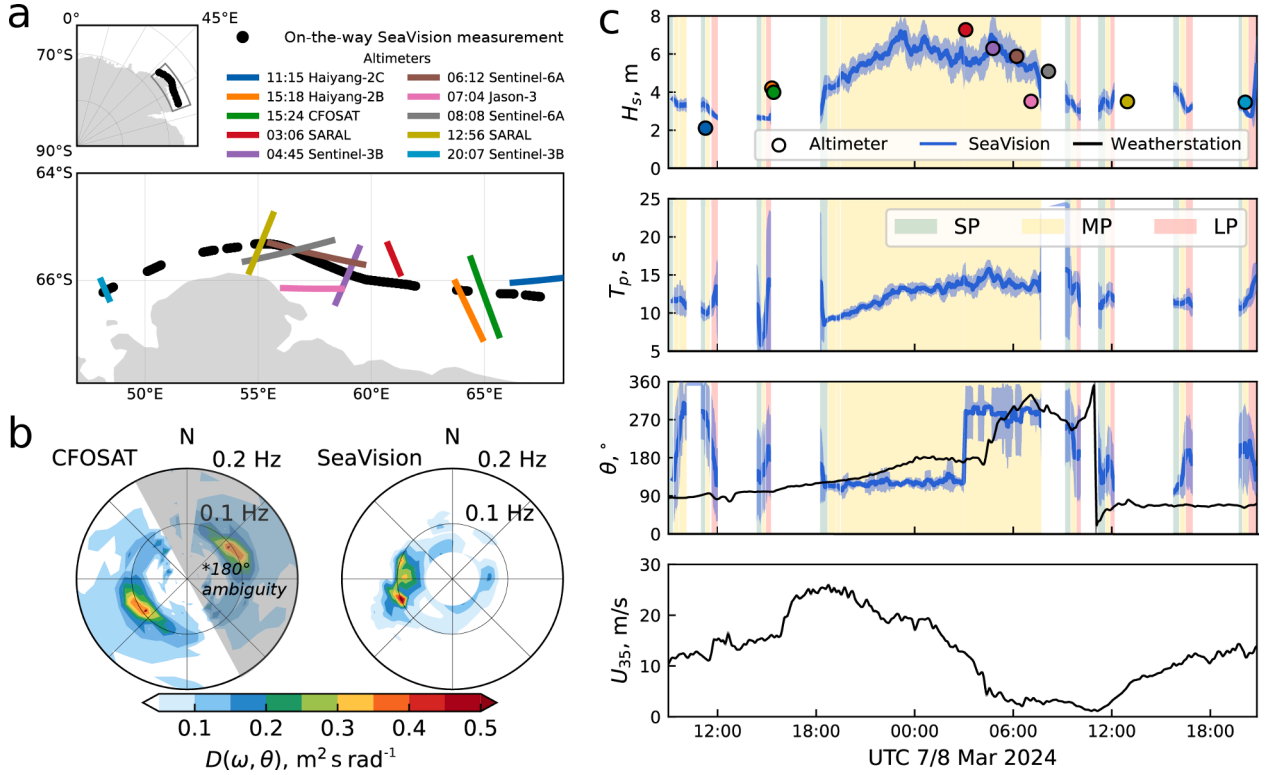

Fig. 7. (a) Underway SeaVision measurements in the Cooperation Sea (Antarctica) on 7 Mar 2024 and in the Cosmonauts Sea 8 Mar 2024 (black dots) with satellite altimeters tracks (color) within a 100 km distance. (b) Directional wave spectra at 15:42 UTC 7 Mar 2024, according to CFOSAT (left) and SeaVision (right) data. As CFOSAT does not identify the wave direction, the mirroring symmetric spectral pattern is masked by light grey. (c) Time series of wave and wind parameters reconstructed using SeaVision (blue) and R/V weather station (black) data. Colors indicate the radar operational mode during data acquisition (green is 8 m spatial resolution, yellow is for 40 m, red is for 180 m).

Antarctica with 7-meter highest SWH, captured at a vessel speed of 15 knots (8 m s^{-1}). The storm evolution was characterized by a growing surface wind speed from 10 to 25 m s^{-1} in the period 10:00–20:00 UTC 7 Mar 2024 after which the wind speed remained higher than 15 m s^{-1} until 02:00 UTC 8 Mar 2024 declining during the next 10 h. SeaVision shows that in response to high winds the waves increased from 2.4–2.9 m to the peak values of 6.8–7.2 m registered at 23:00 7 Mar 2024 and 04:00 UTC 8 Mar 2024. Wind wave periods were in the range between 10 and 16 s progressively increasing during 7–8 March 2024.

During 36 h of measurements, there were as many as 10 cases when the altimeters were within a 100 km distance from the R/V. The comparison of SWH estimations (Fig. 7c) demonstrates a strong agreement, particularly for the closest crossovers (Fig. 7a) with the differences ranging from 10 cm to 80 cm. Remarkably, for the very high wave of about 5.8 m (06:00 UTC 8 Mar 2024) the difference with altimeter data is <20 cm. The analysis was based on Level 3 data from the Copernicus Marine Service (CMEMS, 2025a). During the AF50 cruise, the real-time mode was temporally disrupted and configured manually. Thus, 45-minute SeaVision measurements were performed at different radar pulse modes at locations collocated with satellite altimeter tracks to optimize the data storage. When exceptionally high waves were visually observed, recordings were conducted using the pulse mode selected by the officers or mates (typically the medium pulse mode). This explains discontinuities in the cruise track in Fig. 7a.

Additionally, at 15:42 UTC on March 7, 2024, the CFOSAT mission satellite provided measurements at a point 56 km from the R/V location (CMEMS, 2025b). These measurements also provide spectral wave parameters retrieved from this satellite. Fig. 7b presents a comparison of the two directional wave spectra obtained from CFOSAT (with 180° ambiguity) and SeaVision, showing consistency and even somewhat greater spectral detail in the SeaVision data. It should be noted that SeaVision receives a narrower spectrum than a scatterometer or Spotter buoy (Fig. 4c and Fig. 5c). This is due to the different nature of the measurement methods and the assumptions behind their respective processing algorithms.

SeaVision operates under the standard radar modes of short pulse (SP), medium pulse (MP), and long pulse (LP), which differ in spatial resolution and backscatter quality. The degradation of radar image resolution with increasing pulse length is illustrated in Fig. 2. For routine navigation, MP mode is typically employed, making it the primary setting for SeaVision data acquisition. Despite these differences in resolution, SeaVision demonstrates stable performance across modes, highlighting the robustness of the retrieval algorithm and the potential for dual use of ship radars in both navigation and ocean wave monitoring (Fig. 7c).

A dedicated experiment during the AI65 cruise provided an opportunity to assess this robustness directly. During the station, when R/V and Spotter buoy were drifting, SeaVision measurements were first taken in SP mode. Immediately afterward, the vessel resumed navigation at speeds up to 9 knots (4.5 m s^{-1}), sequentially collecting data in MP and LP modes. Since each radar measurement covered approximately 10 min, the total half-hour period ensured that sea state conditions remained effectively stable, allowing direct validation of underway MP and LP data against the stationary buoy reference. In total, 23 buoy-collocated points were obtained and used to calibrate the SeaVision algorithm. Both the classical linear formula (1) and an extended approach accounting for wind speed (2) were tested. For radar model installed onboard R/V *Akademik Ioffe* SP mode corresponds to 10.5 m in range, MP – 45 m, LP – 120 m

Table 4
Results of comparison of classical (1) and extended (2) empirical parametrization for SWH for different X-band radar operation modes during AI65 buoy-collocated measurements, NRMSE is normalized RMSE.

Radar mode	SP		MP		LP	
Calibration formula	Eq. (1)	Eq. (2)	Eq. (1)	Eq. (2)	Eq. (1)	Eq. (2)
RMSE, m	0.44	0.35	0.63	0.24	0.42	0.38
NRMSE	0.18	0.14	0.19	0.10	0.24	0.16
Bias, m	−0.16	−0.16	−0.02	−0.03	0.19	0.15
Correlation	0.75	0.86	0.63	0.92	0.42	0.86

The results (summarized in Table 4) show significant improvements when wind speed is incorporated, particularly for the LP mode where the initial bias was most pronounced. Interestingly, the bias sign differed between SP and LP, but the unified calibration without mode-specific adjustments yielded an acceptable accuracy across all settings. This is especially important given that the MP mode, which dominates navigational use, exhibited performance metrics superior to those of the classical parametrization (Table 4). When analyzing these improvements, we must take into account the large differences in sample sizes; however these findings confirm that SeaVision retrievals remain reliable across different radar operational modes, reinforcing its applicability for global-scale deployment where radar settings may vary from ship to ship.

An overall intercomparison of all underway SeaVision measurements was performed for all 28 TB SeaVision wave data consisting of >1200 h of measurements. Co-location uncertainties in both time and space place an obvious constraint on direct comparisons. While altimeters tracks provide SWH averaged over several kilometers, SeaVision captures wave height at a much finer resolution (~40 m in MP mode).

The results of the overall comparison of SeaVision underway measurements with co-located altimeter data (Fig. 8a) demonstrate very good agreement, with no significant bias but scattering characterized by RMSE of 0.67 m. A key challenge in analyzing collocation measurements is the increase in estimated errors with expanding the spatial search window (Fig. 8b). Therefore, it is essential to balance the required number of points with acceptable error bounds. Altimetry data processing algorithms also introduce an error of approximately 20 cm (Taburet et al. 2023), which contributes to the total RMSE. The standard approach is to use a 50 km spatial window for crossover analysis, which can be extended to 200 km in cases of sufficiently homogeneous wind fields (Ezhova et al. 2024). In this study, a larger window was chosen to increase the sample size.

4. Comparison with co-located visual VOS data

We also provided a comparison of SeaVision wave measurements with limited sub-sets of visual VOS observations. Visual wind wave observations are consolidated in the International Comprehensive Ocean-Atmosphere Data Set (ICOADS, Freeman et al. 2017, Liu et al. 2022). These data represent visual estimates of wind sea and swell heights with observational accuracy of 0.5 m (0.5 m increments) as well as sea and swell periods with a reported accuracy of 1 s and directions (reported accuracy is 10 degrees). Here the comparison was performed for SWH which was computed from the VOS observations according to Gulev et al. (2003) as the highest of the two components. Alternative (and somewhat more accurate) estimates of SWH could be derived from sea height h_w and swell height h_s as $SWH = \left(h_w^2 + h_s^2\right)^{1/2}$ or using a combined approach, accounting for sea and swell directions (Gulev and Hasse 1998; Gulev et al. 2003). However, in the used subsets of visual observations the information about sea and swell was present in <3 % of reports, thus a simplified algorithm was used. Quality control of visual wave observations was applied according to Gulev et al. (2003) and included multiple quality checks based upon statistical measures, joint consideration of heights and periods and of surface wind and wave parameters (wave age). The two sub-sets of visual wave observations were analyzed (Table 5). One included visual observations performed by officers of the R/V where SeaVision data were collected and another included visual observations of VOS in the vicinity of R/Vs carrying SeaVision equipment. For the first subset we considered separately observations fully collocated in space and time (225 observations) and

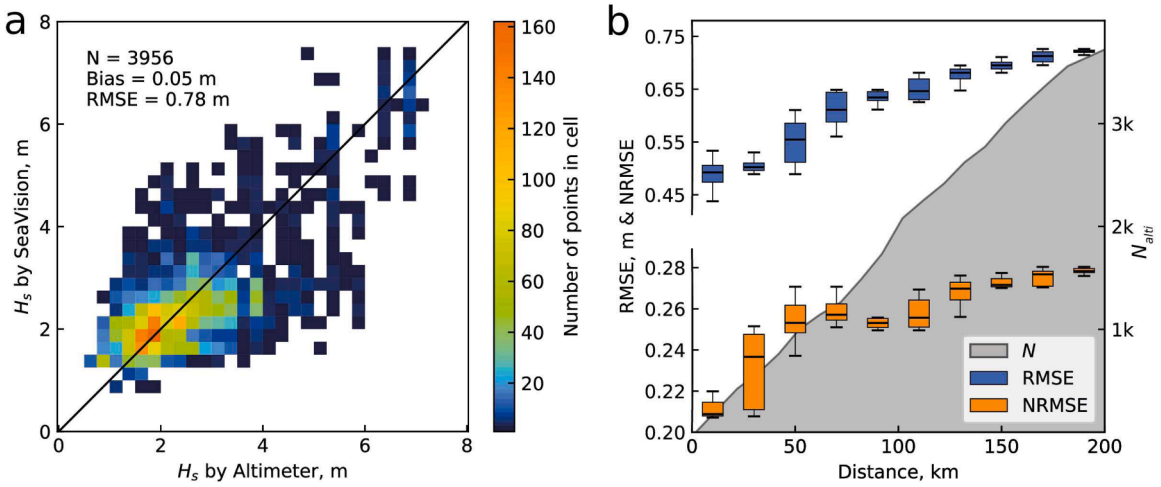

Fig. 8. (a) Scatter plot of SWH obtained by altimeter and retrieved by SeaVision algorithm, *N* is the number of validation segments. (b) Dependence of SWH estimation RMSE and NRMSE on the distance between the measurements point of the SeaVision and the altimeter, grey filling shows total number of samples co-located with altimetry data.

Table 5
Results of comparison of SWH measured by SeaVision with the other data sources.

Data source	Spotter buoy	Satellite altimetry		Visual observations				
Collocation	**fully collocated**	**30 km distance, ±2 h time window**	**200 km distance, ±2 h time window**	**Fully collocated in space and time**	**Collocated in space, ±2 h time window**	**30 km distance, ±2 h time window**	**200 km distance, ±2 h time window**	**All VOS observations**
Number of pairs	1174	550	3956	225	129	26	277	631
RMSE, m	0.44	0.50	0.78	0.69	0.75	0.63	0.79	0.75
NRMSE	0.20	0.21	0.29	0.35	0.28	0.21	0.34	0.33
Bias, m	0.02	0.09	0.05	−0.34	−0.23	0.00	−0.20	−0.26
Correlation	0.75	0.75	0.74	0.58	0.75	0.75	0.60	0.62

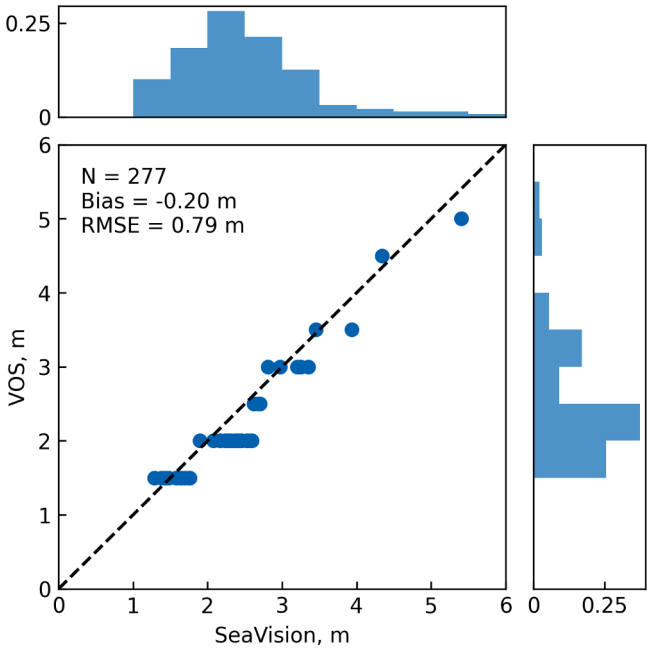

Fig. 9. Q-Q plot of SWH estimated by SeaVision versus reported by VOS for ±2 h time window and a maximum vessel separation of 200 km. The top and right panels show the probability density distribution of SWH from SeaVision and VOS respectively.

those collocated in space but collected within ± 2 h time window taken (129 observations). For VOS observations by the neighboring commercial ships we considered observations collected within ± 2 h time window and within 30 km and 200 km distances from the R/V holding SeaVision (Table 5).

Table 5 shows that SeaVision SWH measurements fit reasonably well to visual estimates. For reference we show in Table 4 also statistics of comparison with Spotter buoy data (Section 3.1) and with satellite altimeter data (Section 3.3). Visual observations report 0.2–0.3 m smaller SWH compared to SeaVision while for the VOS data collected within 30 km distance the bias was zero. Normalized RMSE is slightly larger for VOS vs SeaVision comparison than for comparison of SeaVision data with altimetry and Spotter buoy and correlations are very close for the comparisons with VOS and with satellite data. Fig. 9 shows a Q-Q plot of SeaVision and VOS data collected within 200 km distance and ± 2 h time window. Interpretation of the Q-Q plot should account for different observational precisions of VOS estimates and SeaVision measurements. Nevertheless, Fig. 8 clearly shows that SWH estimates reported by VOS are close to SeaVision measurements with underestimation of about 0.2 m even for distances within 200 km. This bias is smaller than observational accuracy of visual measurements estimated using semivarigram approach by Gulev et al. (2003).

Overall, comparison of SeaVision measurements with a limited subset of visual VOS data demonstrates that the two data sources are quite consistent with each other and further validation using larger subsets of VOS observations can provide robust relationships between VOS and SeaVision data.

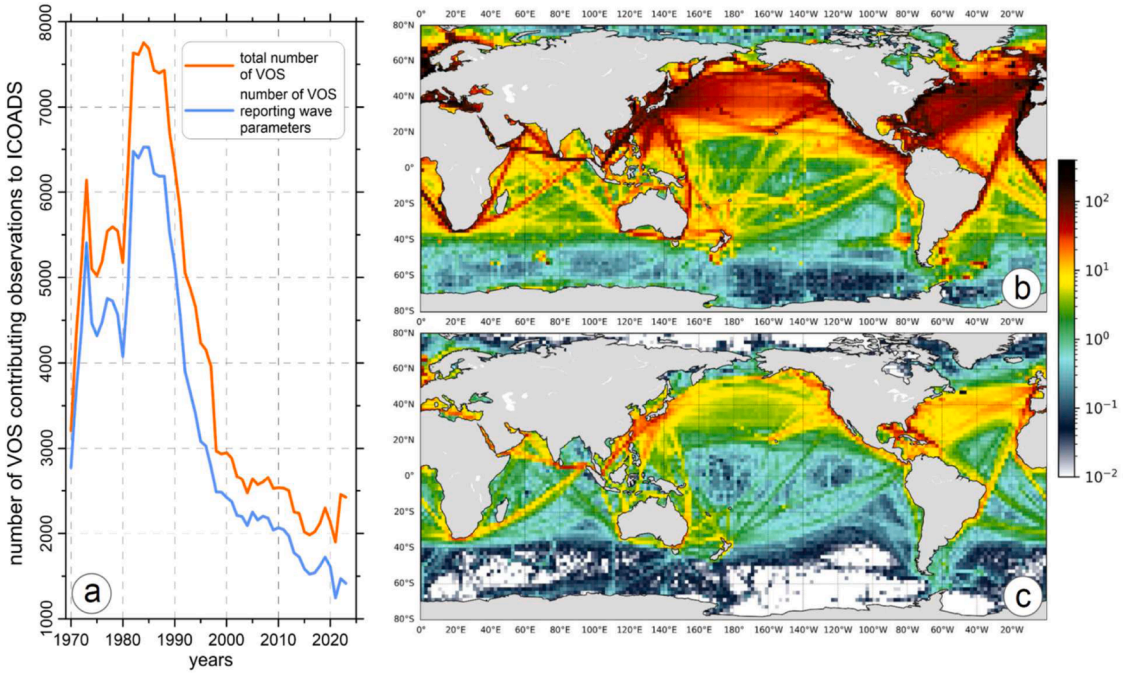

Fig. 10. (a) Historical changes in the number of VOS contributing observations to ICOADS and the number of VOS reporting wind wave observations. (b) The total number of VOS reports (per 2-degree box per month) in the period 1970–1990. (c) The number of VOS reports containing wave information (per 2-degree box per month) in the period 2000–2023.

5. SeaVision potential for a global wind wave observing system

SeaVision opens an avenue for developing a truly global wind wave operational observing system. This is an extremely important challenge given the rapidly declining health of the existing open ocean observing systems, first of all the VOS (Kent et al. 2019; Smith et al. 2019). For many decades VOS wind wave observations provided a critically important source of wind wave data in the open ocean. However, the 1990s marked an obvious sunset of the earlier 'golden age' of the VOS observing system. Fig. 10 demonstrates how the number of VOS reporting on GTS and contributing to the ICOADS declined from 5500–7800 ships in the late 1970s and 1980s to <3000 in the late 1990s and continued to further decrease to about 2000–2200 in the 2010s.

Several factors contribute to this trend. The shipping industry saw a consolidation toward larger carriers (especially tankers and container ships), resulting in fewer vessels overall. The installation of automated weather systems on many ships in the 1990s reduced the need for bridge officers to submit manual/visual observations — including visual wind wave data — leading to even sharper reductions in report frequency. Similar declines were reported for visual cloud cover observations (Aleksandrova et al. 2018). Fig. 10a shows that the number of ships reporting visually observed waves declined even at a faster pace compared to the total number of VOS. If we consider the number of individual reports (no figure shown), there will be even a tendency of an increasing total number of VOS reports after 2000. However, this increase is the result of the massive installation of automated weather stations reporting a very limited set of the parameters (mostly SLP and air temperature). At the same time the number of extended individual VOS reports with wind wave information continues to decline.

The current number of commercial ships forming everyday ship traffic on the world ocean amounts to slightly over 106,000 vessels (Atlas Magazine, 2024), while the UN Trade and Development (UNCTAD, 2024) gives a slightly lower number of 102,000 vessels. Considering fishery ships, these estimates account for only motorized decked vessels with the deadweight tonnage (DWT) higher than 100, as the total number of fishing ships exceeds 3 million (FAO, 2024). Assuming SeaVision or similar system being installed on at least 10 % of all carriers reporting during 30 % time of the year (estimate based on VOS), this will result in >120 million 10-minute reports of wave parameters including 2D spectra per year. Scaling this number to 6-hourly time intervals (VOS ship reporting frequency) this gives an equivalent of about 3 million reports per year largely exceeding the capacity of VOS even in the 1980s.

This loss translates into a significant decrease in data density. Figs. 10b, 10c show that the number of VOS wave reports in the North Atlantic and North Pacific declined from 150–600 to 40–100 per month per 2°-box between 1970s-1980s and 2000s-2020s. The decline in the Southern Ocean was from few tens to 0–5 per month per 2-degree box. Overall the annual number of wind wave reports declined from 2–2.2 million a year during the 1980s to <400,000 in the recent years. Note that the decline in the number of reports is even stronger compared to the change in the number of reporting ships, as many officers and mates stopped to use a standard 6-hourly reporting time switching to less frequent reporting (typically 12-hourly). Moreover, if we consider reports containing full sets of wind wave variables (heights, periods and directions of wind waves and swell), the annual estimates will be even about 40–50 % smaller (Grigorieva et al. 2022).

In recent years, the deployment of Sofar Spotter buoys (Raghukumar et al., 2019) has partially alleviated the decline of in situ wind wave observations following the declining tendency of VOS observations in general. Spotters are compact, solar-powered platforms capable of transmitting real-time measurements of SWH, mean and peak wave periods, wave direction and spreading, atmospheric pressure, sea surface temperature (SST), and wind speed and direction via the Global Telecommunication System (GTS) at intervals of 30 to 60 min. Since their first deployment in 2017, the Spotter network has expanded to

approximately 500–600 active buoys, primarily concentrated along major mid-latitude ocean currents and coastal regions (https://weather.sofarocean.com). High-resolution datasets, including hourly wave spectral records for the 2019–2022 period, are publicly available.

Despite these advantages, Spotter buoys remain insufficient for filling the observational gap left by VOS. Their spatial distribution is highly uneven, with sparse coverage across the central ocean basins, polar regions, and the Southern Hemisphere. This limited deployment footprint hampers their utility for global wind wave monitoring. Additionally, the operational lifetime of Spotter buoys is constrained: while nominal lifetimes range from several months to a few years, actual durations are often shorter due to exposure to harsh sea states, biofouling, power limitations, and accidental recovery or loss. This restricts long-term, consistent data collections in remote regions where retrieval and maintenance are challenging.

The National Data Buoy Center (NDBC) presently maintains a network of approximately 1000 moored buoys globally (https://www.ndbc.noaa.gov/). However, only few of these buoys are equipped with wave sensors. Most NDBC buoys are located near coastal zones, limiting their capability for open-ocean wave climate monitoring. These limitations emphasize that the current buoy networks — although valuable — are still insufficient to meet the requirements for global-scale wind wave observing.

In this respect the potentially massive installation of the SeaVision packages onboard of commercial vessels will significantly contribute to the increasing sampling density of wave observations of the global ocean. At the projected low cost of SeaVision (or similar systems) they become attractive for the owners of marine carriers. Importantly, such a system onboard commercial ships will be beneficial for officers, as it also allows for providing additional valuable real-time information about the marine environment, such as sea ice, surface currents and potentially oil spills.

For transmitting the SeaVision data on GTS standard formats and requirements are available (WMO 2023) to ensure rapid and reliable submission to real-time users. Thus, the massive implementation of SeaVision onboard of commercial vessels can establish in the future a global observational network of wind waves as a part of GCOS and GOOS of the World Meteorological Organizations (WMO) and Intergovernmental Oceanographic Commission (IOC). GCOS Implementation Plan (Zemp, 2022) considers the ocean sea state among the so-called Essential Climate Variables (ECV). ECVs according to GCOS are those that critically contribute to the characterization of Earth's climate. For instance, for the wave height GCOS defines requirements (Ardhuin et al. 2019) which are not currently satisfied by observing systems. Both operational systems GOOS and GCOS provide the necessary infrastructure to collect and distribute these products in real-time to end-users. SeaVision data will cover the presently existing deficit both in areal and temporal coverage of the ocean. In the end this will support improving products that describe at a qualitatively high and uniform level the state of the ocean, an important part of the Earth system.

6. Conclusions

We presented SeaVision, an automated, cost-effective system attachable to standard shipborne navigation radars, enabling the continuous and real-time measurement of wind wave parameters, including directional spectra. Using onboard processing of radar backscatter and optional GTS transmission, SeaVision supports customizable data resolution and volume, allowing seamless integration into existing maritime operations.

While standard navigation radars have some limitations associated particularly with the cut-off of resolution compared to separately installed commercial systems, their advantage is their availability on every vessel and thus the potential increase of usable platforms to provide massive additional observations. Our work shows that these limitations could be partly minimized using calibration of measurements taken in different pulse modes (Section 3.3, Table 4).

Through case studies in diverse ocean environments and validation against Spotter buoys and satellite altimetry, we demonstrated the capability of SeaVision to provide high-quality in situ wave observations. With over 1000 h of archived data, the system has proven robust across variable sea states and vessel types.

Given the continued decline of ship-based visual observations (VOS) and limited global buoy coverage, SeaVision offers a scalable alternative. Its potential for widespread deployment aboard merchant vessels positions it as a valuable contributor to global ocean observing systems such as GOOS and GCOS, addressing Essential Climate Variables (ECVs) like sea state.

Further developments of SeaVision to be provided in the near future will include the possibility to retrieve surface wind, surface currents, detecting oil spills and charting sea ice (for which SeaVision is set already). Wind direction is determined by identifying the azimuth and range of the brightest region in the radar image (Dankert et al. 2003; Lund et al. 2012; Vicen-Bueno et al. 2013). Sea ice detection is based on averaging time series and compiling snapshots (Ermoshkin and Molkov, 2022), making it well-suited for machine learning applications, while drift speed estimation has already been established (Lund et al. 2018a). Surface currents are derived by analyzing the Doppler shift in the dispersion relation (Young et al. 1985; Lund et al. 2015; Lund et al. 2018b). SeaVision has also been used to detect internal wave signatures by analyzing surface roughness variance (Lund et al., 2013; Celona et al. 2021; Kozlov et al. 2023), a process that, like the detection of oil slicks (Li et al. 2022) and artificial slicks (Ermoshkin et al. 2019), will be further automated.

SeaVision thus represents a promising path toward a truly global, shipborne in situ network for real-time remote sensing of the ocean surface.

Data availability

The SeaVision dataset, available at https://sail.ocean.ru/EzhovaSeaVision/, includes 10-minute mean wind wave characteristics such as significant wave height (SWH), peak wave period, and mean wave direction, as well as directional wave spectra with 25 frequency bins and 36 directional bins. The dataset spans the period 2020–2025 and is regularly updated. Built-in software realizing all stages of pre-processing and SeaVision algorithms in the form of Python codes and platform independent executable files are also available on the SeaVision portal.

All SeaVision outputs are provided as NetCDF files, each corresponding to one cruise. These files are supplemented with weather station data (surface temperature, SST, sea level pressure, humidity, wind speed) and with visual observations of the present and past weather and environmental conditions such as precipitation, wind state, visibility, ice conditions.. The full archive currently comprises approximately 150 terabytes, with individual files ranging from 4 to 40 GB. Researchers interested in accessing the full raw radar dataset may contact Alexander Gavrikov at gavr@sail.msk.ru to request access.

A curated subset of SeaVision data is openly accessible through the PANGAEA repository Gavrikov et al. (2021) (for cruises before 2022) and has been expanded in Ezhova et al. (2025).

CRediT authorship contribution statement

Elizaveta Ezhova: Writing – review & editing, Writing – original draft, Visualization, Validation, Software, Methodology. **Natalia Tilinina:** Writing – review & editing, Supervision, Project administration, Investigation, Funding acquisition, Conceptualization. **Sergey Gulev:** Writing – review & editing, Writing – original draft, Supervision, Funding acquisition, Conceptualization. **Vitali Sharmar:** Validation, Methodology. **Alexander Gavrikov:** Software, Methodology, Data curation. **Boris Trofimov:** Resources, Methodology. **Sergey Bargman:** Resources, Methodology. **Peter Koltermann:** Writing – review &

editing. **Vika Grigorieva:** Visualization, Validation, Data curation. **Alexander Suslov:** Data curation.

Declaration of competing interest

The authors declare that they have no known competing financial interests or personal relationships that could have appeared to influence the work reported in this paper.

Acknowledgements

This work was supported by the RF National Climate Program supported by Russian Metoffice, Ministry of Science and Higher Education and Ministry of Economic Development under the FMWE-2025–0002 and by RSF grant # 23–77–30001. Logistics of SeaVision underway observations was supported by the Russian Antarctic Expedition under the project 169–00015–24–00 funded by Russian National Metoffice. We greatly appreciate support from IORAS and AARI administrations as well as the crews of R/V *Akademik Sergey Vavilov*, R/V *Akademik Ioffe* and R/V *Akademik Fedorov* for their support in setting up SeaVision hardware and the organization of Spotter buoy measurements in the open ocean. We greatly appreciate the suggestions and criticism of the editor and two anonymous reviewers on the first version of the manuscript. Specific thanks go to Alexey Sokov, who supported the SeaVision development at the initial stage and to Vasilisa Koshkina, Vsevolod Gladyshev, Mikhail Krinitskiy, Mikhail Kalinin, Maria Artemieva who contributed to the SeaVision data collection onboard R/Vs.

Appendix A. Description of SeaVision algorithm

The SeaVision algorithm (as noted above, Section 2) consolidates different advantages of several algorithms for the radar image processing reviewed by Huang et al. (2017). The algorithm allows for retrieving from the raw radar images providing basic variables of wind waves (height, period and direction) as well as 1D and directional spectra. Fig. A1 shows the flowchart of the algorithm whose details are described below.

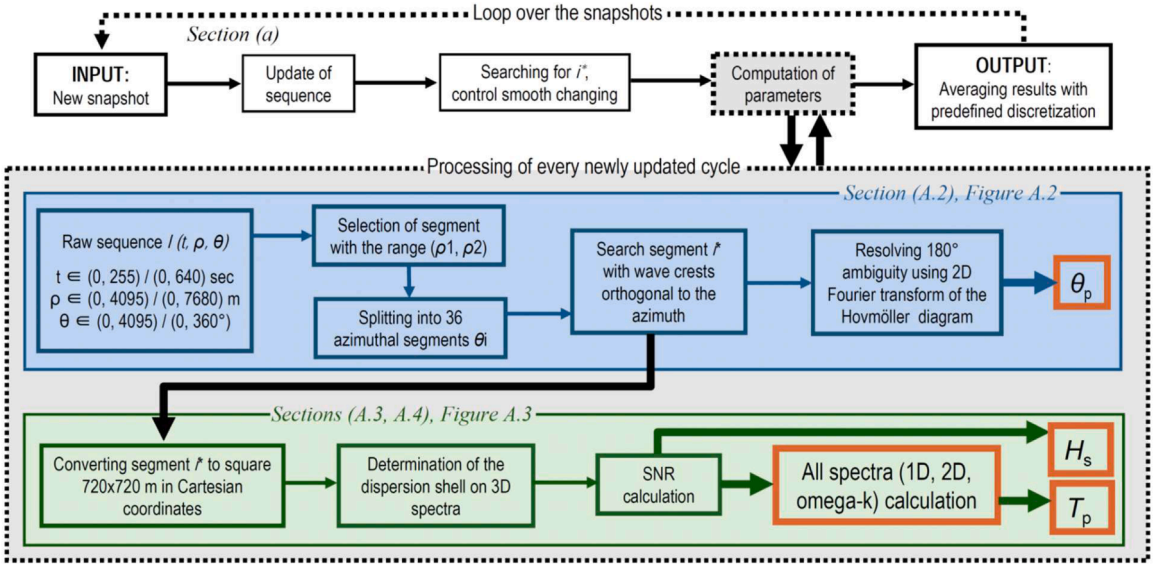

Fig. A1. Flowchart diagram of SeaVision algorithm.

A.1. Initial processing of the radar images

Let $I(t, \rho, \theta)$ be the initial time series of the intensity of the radar signal reflected from the sea surface in polar coordinates, where ρ is the range and θ is the azimuth, t is time. The raw radar image is highly anisotropic in azimuth (Lund et al. 2014; Støle-Hentschel et al. 2024). Following the methodology (Lund et al. 2014) a segment of size 384 × 384 px (corresponding to 720 × 720 m), is extracted and converted into Cartesian coordinates. Typically, the most representative segment is the one where wave crests are orthogonal to the radar beam. For real-time processing, a sequence of 256 radar images is used, updating cyclically with each antenna rotation. If necessary (e.g., for averaging), the algorithm can be loaded with any dataset.

A.2. Wave direction estimation

First, the original dataset $I(t, \rho, \theta)$ is restricted to the range $\rho \in (\rho_1, \rho_2)$, where $\rho_1 = 765$ m, $\rho_2 = 1485$ m (Fig. A2a), because it contains the highest contrast signal (Ezhova et al. 2024). Then the data are divided into 36 equal azimuthal segments, with $q_i = i \cdot 10°$, $i \in \{0, 35\}$ (Fig. A2b). For each segment, azimuthal integration is performed (Fig. A2c):

$$R(t,\rho) = \int_{\theta_i}^{\theta_{i+1}} I(t,\rho,\theta)\mathrm{d}\theta. \tag{A1}$$

After that we compute the variance $s_i(t)$ over the range (ρ_1, ρ_2) (Fig. S1d):

$$s_i^2(t) = \frac{1}{\rho_2 - \rho_1}\int_{\rho_1}^{\rho_2}\left(R_i(t,\rho) - \frac{1}{\rho_2 - \rho_1}\int_{\rho_1}^{\rho_2} R_i(t,\rho)d\rho\right)^2 d\rho. \quad (A2)$$

The estimated wave direction θ^* (with 180° ambiguity) is determined as:

$$\theta^* = 10^\circ \cdot i^* = 10^\circ \cdot \underset{i}{argmax}\left(\int s_i(t)dt\right). \quad (A3)$$

To resolve the 180° ambiguity, a Hovmöller diagram is computed for $R_{i^*}(t, \rho)$ (Fig. A1e). The inclination of wave crest projections (either positive or negative) indicates that waves moved closer or further away from the radar. This inclination is estimated using a 2D Fourier transform that computes the ω-k spectrum (Fig. A2f).

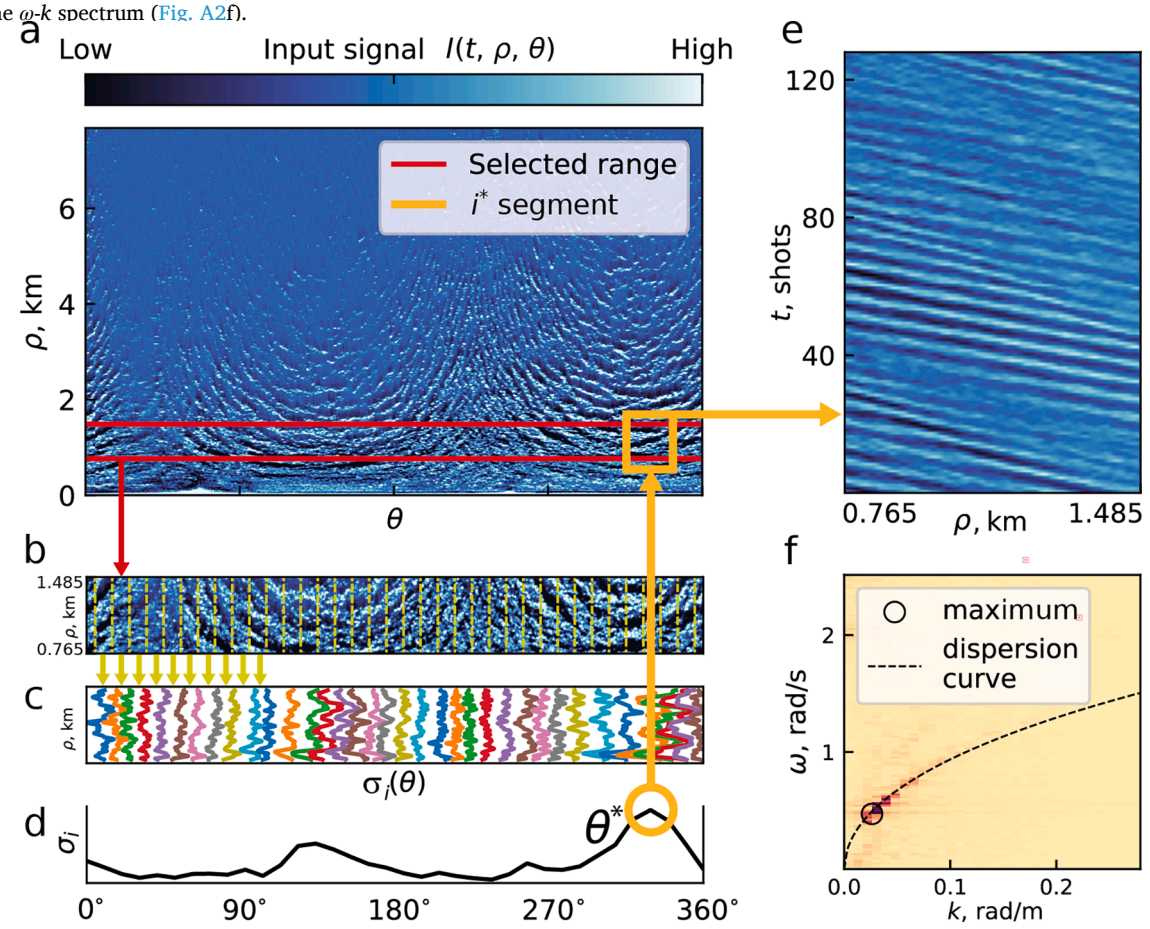

Fig. A2. (a) Single radar image in polar coordinates across the entire available region, with the selected range (ρ_1, ρ_2). (b) Extracted range with 36 azimuthal segments (dashed yellow). (c) Azimuthal integration for each segment $s_i(\rho)$, 36 color lines correspond to each segments. (d) Variance of the summed signal for each segment $R(\theta)$. (e) Hovmöller diagram of the summed signal for the selected azimuth θ^* (orange on a and b). (f) ω-k pattern of the Hovmöller diagram, showing the maximum point (circle) and the fitted dispersion curve (dashed line).

A.3. Processing of the selected square

To compute the wave spectrum, a 384 × 384 px (720 × 720 m) segment is extracted from each of the 256 snapshots, centered at $0.5(\rho_1 + \rho_2) = 600$ px (1125 m) along the azimuth θ^* (Fig. A3a). The segment is then transformed into Cartesian coordinates (x, y), where y is aligned with azimuth θ^* and x is orthogonal to it (Fig. A3b). A 2D FFT is applied then in space domain, being followed by a Welch transform in time (Tilinina et al. 2022). At this stage the resulting 3D spectrum $S(\omega,k,\theta)$, where ω is the temporal frequency, and k is the wave number, is analyzed to identify the dispersion shell (Young et al. 1985) (Fig. A3c) satisfying the deep-water wave dispersion relation:

$$\omega = \sqrt{gk} + kV\cos\varphi, \quad (A4)$$

where g is gravity acceleration, V is modulus of vector **V** includes ship velocity, current velocity and other typically smaller components, φ is the angle between the wave vector and **V**. The term $kV\cos\varphi$ is estimated by fitting the curve (A4) at the origin and the maximum point of $S(\omega, k)$ (Fig. A2f, A3d), which calculated as

$$S(\omega,k) = \int_0^{2\pi} S(\omega,k,\theta)d\theta. \quad (A5)$$

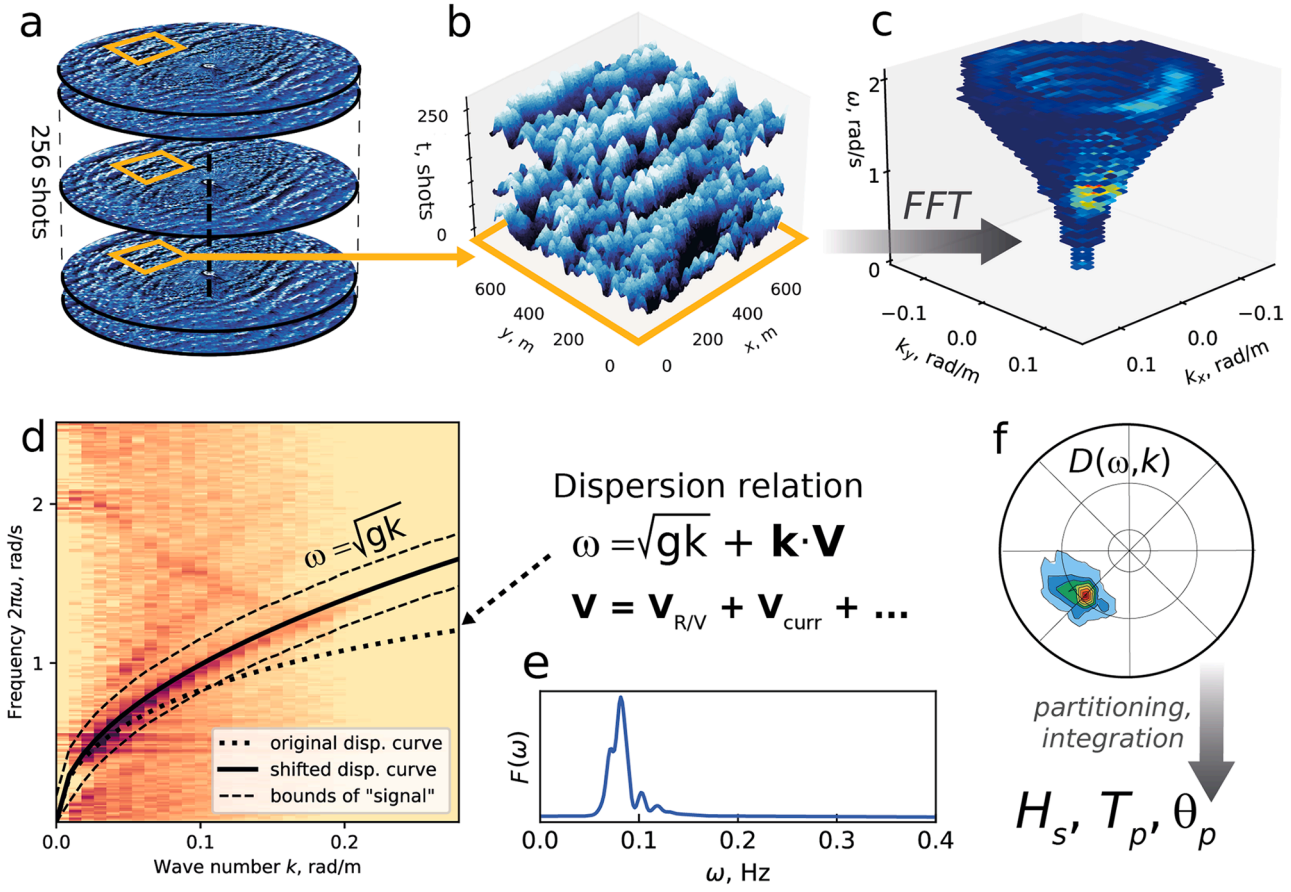

Fig. A3. (a) Number of radar image frames in polar coordinates, with the selected square (orange) for further processing. (b) Sequence of radar frames extracted from the selected square (orange on a). (c) Identified dispersion shell extracted from 3D spectrum. (d) ω-k spectrum with the dispersion curve in the stationary frame (solid line), and its original position in the moving frame (dotted line) with dispersion shell boundaries indicated (dashed line), (e) Frequency spectrum, (f) Directional spectrum.

A.4. Spectra calculation

The Doppler correction estimated in Section 2 is used to refine the position of the dispersion shell, ensuring that the final wave spectra correspond to a stationary reference frame (Collins III et al. 2017). The dispersion shell is then classified as the signal domain, while all other components are considered to be noise, also low frequency areas $\omega < \omega_l$ are considered as noise. The highest frequency ω_h is determined by the antenna rotation speed. The shell width is selected equal to 0.025 Hz. A modulation transfer function $k^{-1.2}$ is applied, where the degree of 1.2 was chosen as a hyperparameter for the processing and coincided with that proposed in (Nieto-Borge et al. 2000):

$$S(\omega,\theta) = \int_{in\ shell} S(\omega,\mathrm{k},\theta)k^{-1.2}d\mathbf{k}. \tag{A6}$$

The frequency spectrum $F(\omega)$ is computed as:

$$F(\omega) = \int_0^{2\pi} S(\omega,\theta)d\theta, \tag{A7}$$

and the directional spectrum $D(\omega,\theta)$ as:

$$D(\omega,\theta) = \frac{S(\omega,\theta)}{F(\omega)}. \tag{A8}$$

The peak frequency ω_p=argmax $F(\omega)$, peak period $T_p = 2\pi\ /\omega_p$ and mean wave period T_{m01}:

$$T_{m01} = 2\pi\frac{\int F(\omega)d\omega}{\int F(\omega)\omega d\omega}, \tag{A9}$$

is estimated from the frequency spectrum. From directional spectrum we obtain bulk parameters $a(\omega)$, $b(\omega)$, their averages a_m, b_m:

$$a(\omega) = \int_0^{2\pi} D(\omega,\theta)\cos\theta d\theta, b(\omega) = \int_0^{2\pi} D(\omega,\theta)\sin\theta d\theta,$$
$$a_m = \int a(\omega)d\omega, b_m = \int b(\omega)d\omega, \tag{A10}$$

and calculate the peak direction $\theta_p = \arctan2(b(\omega_p), a(\omega_p))$, mean direction $\theta_m = \arctan2(b_m, a_m)$, peak σ_p and mean spreading σ_m:

$$\sigma_p = \sqrt{2 - 2\left(a(\omega_p)^2 + b(\omega_p)^2\right)^{1/2}}, \sigma_m = \sqrt{2 - 2\left(a_m{}^2 + b_m{}^2\right)^{1/2}}. \tag{A11}$$

Finally, the significant wave height is estimated using the Eq. (1) from Nieto-Borge et al. (1999), where *SNR* calculated as:

$$SNR = \frac{\int_{\omega_l}^{\omega_h}\int_0^{2\pi} S(\omega,\theta)d\theta d\omega}{\int_{\omega_l}^{\omega_h}\int_{out\ of\ shell} S(\omega,k)dkd\omega}, \tag{A12}$$

where *A, B* are predominant calibration coefficients determined in advance, based on the characteristics of radar and validated using buoy data. For some cases when reliable weather station data is available instead of (1), the empirical parametrization (2) taking into account the wind speed is used. All subsequent calculations are independent of these parameters. Since $H_s{}^*=4m_0^{1/2}$ where the zeroth moment of the spectrum m_0 defining as

$$m_0 = \int F(\omega)d\omega, \tag{A13}$$

the conversion coefficient to energy units in (A7) is computed as $(H_s{}^* / H_s)^2$.

A.5. Real-time processing details

In continuous operation, the algorithm processes a sequence of 256 sequential radar images with the specified discretization. The results are averaged over 3–5 consecutive executions of the algorithm. Instead of storing the full dataset (4 GB) in RAM, only the extracted squares (~30 MB) are retained. To prevent artificial discontinuities when merging different image segments, the algorithm restricts abrupt changes in θ^*. For consecutive frames, is allowed to shift only by one adjacent segment. If a pulse change occurs, the affected frame is excluded from processing. When starting, the required number of pictures is accumulated, so the first results can be obtained with a delay of about 10 min after turning on (depending on the number of images processed, i.e. temporary resolution).

References

Aleksandrova, M., Gulev, S.K., Belyaev, K., 2018. Probability distribution for the visually observed fractional cloud cover over the ocean. J. Climate 31, 3207–3232. https://doi.org/10.1088/1755-1315/231/1/012005.

Al-Habashneh, A.-A., Moloney, C., Gill, E.W., Huang, W., 2018. The effect of radar ocean surface sampling on wave spectrum estimation using X-band marine radar. IEEE Access 6, 17570–17585. https://doi.org/10.1109/ACCESS.2018.282156.

Ardhuin, F., Stopa, J.E., Chapron, B., Collard, F., Husson, R., Jensen, R.E., et al., 2019. Observing sea states. Front. Mar. Sci. 6, 124. https://doi.org/10.3389/fmars.2019.00124.

Aouf, L., Hauser, D., Chapron, B., Toffoli, A., Tourain, C., Peureux, C., 2021. New directional wave satellite observations: towards improved wave forecasts and climate description in Southern Ocean. Geophys. Res. Lett. 48, e2020GL091187. https://doi.org/10.1029/2020GL091187.

Atlas Magazine, 2024. The world merchant fleet. https://www.atlas-mag.net/en/category/tags/focus/the-world-merchant-fleet accessed 22 March 2025.

Babanin, A.V., Onorato, M., Qiao, F., 2012. Surface waves and wave-coupled effects in lower atmosphere and upper ocean. J. Geophys. Res. Oceans 117, C00J01. https://doi.org/10.1029/2012JC007932.

Babanin, A.V., Rogers, W.E., de Camargo, R., Doble, M., Durrant, T., Filchuk, K., et al., 2019. Waves and swells in high wind and extreme fetches, measurements in the Southern Ocean. Front. Mar. Sci. 6, 361. https://doi.org/10.3389/fmars.2019.00361.

Bitner-Gregersen, E.M., Gramstad, O., Magnusson, A.K., Malila, M., 2020. Challenges in description of nonlinear waves due to sampling variability. J. Mar. Sci. Eng. 8, 279. https://doi.org/10.3390/jmse8040279.

Buckley, J.R., Allingham, M., Michaud, R., 1994. On the use of marine radar imagery for estimation of properties of the directional spectrum of the sea surface. Atmos. Ocean 32, 195–213. https://doi.org/10.1080/07055900.1994.9649495.

Buckley, J.R., Aler, J., 1998. Enhancements in the determination of ocean surface wave height from grazing incidence microwave backscatter. IGARSS'98 IEEE Int. Geosci. Remote Sens. Symp. Proc 5, 2487–2489. https://doi.org/10.1109/IGARSS.1998.702254.

Carrasco, R., Horstmann, J., Seemann, J., 2017. Significant wave height measured by coherent X-band radar. IEEE Trans. Geosci. Remote Sens. 55, 5355–5365. https://doi.org/10.1109/TGRS.2017.2706067.

Cavaleri, L., Fox-Kemper, B., Hemer, M., 2012. Wind waves in the coupled climate system. Bull. Am. Meteorol. Soc. 93, 1651–1661. https://doi.org/10.1175/BAMS-D-11-00170.1.

Celona, S., Merrifield, S.T., de Paolo, T., Kaslan, N., Cook, T., Terrill, E.J., Colosi, J.A., 2021. Automated detection, classification, and tracking of internal wave signatures using X-band radar in the inner shelf. J. Atmos. Oceanic Technol. 38, 789–803. https://doi.org/10.1175/JTECH-D-20-0129.1.

Collard, F., Ardhuin, F., Chapron, B., 2005. Monitoring and analysis of ocean swell fields from space: new methods for routine observations. J. Geophys. Res. Oceans 114, C07023. https://doi.org/10.1029/2008JC005215.

Collins III, C.O., Blomquist, B., Persson, O., Lund, B., Rogers, W.E., et al., 2017. Doppler correction of wave frequency spectra measured by underway vessels. J. Atmos. Oceanic Technol. 34, 429–436. https://doi.org/10.1175/JTECH-D-16-0138.1.

Collins, C.O., Rogers, W.E., Marchenko, A., Babanin, A., 2018. Observations of surface wave dispersion in the marginal ice zone. J. Geophy. Res. 123 (1), 333–346. https://doi.org/10.1029/2018JC013788.

Collins, C.O., 2025. Measuring ocean surface waves. ESS Open Archive. https://doi.org/10.22541/essoar.175130482.28547248/v1. *Submitted to* Reviews of Geophysics.

Cornejo-Bueno, L., Borge, J.N., Alexandre, E., Hessner, K., Salcedo-Sanz, S., 2016. Accurate estimation of significant wave height with support vector regression algorithms and marine radar images. Coastal Eng. 114, 233–243. https://doi.org/10.1016/j.coastaleng.2016.04.007.

Chen, Z., Zhang, B., He, Y., Qiu, Z., Perrie, W., 2015. A new modulation transfer function for ocean wave spectra retrieval from X-band marine radar imagery. Chin. J. Oceanol. Limnol. 33, 1132–1141. https://doi.org/10.1007/s00343-015-4147-1.

Chen, Z., Chen, X., Zhao, C., Wang, Z., 2019. Wave height and wave period derived from a shipboard coherent S-band wave radar in the South China Sea. Remote Sens. 11, 2812. https://doi.org/10.3390/rs11232812.

Chernyshov, P., Vrecica, T., Toledo, Y., 2018. Inversion of nearshore X-band radar images to sea surface elevation maps. Remote Sens. 10, 1919. https://doi.org/10.3390/rs10121919.

CMEMS, 2025a. Global Ocean L3 significant wave height from NRT satellite measurements. https://doi.org/10.48670/moi-00179 (accessed 22 March 2025).

CMEMS, 2025b Global Ocean L3 spectral parameters from NRT satellite measurements. https://doi.org/10.48670/moi-00178 (accessed 22 March 2025).

Dankert, H., Horstmann, J., Rosental, W., 2003. Ocean wind fields retrieved from radar-image sequences. J. Geophys. Res. 108 (C11), 3352. https://doi.org/10.1029/2003JC002056.

Dankert, H., Horstmann, J., Rosental, W., 2005. Wind- and wave-field measurements using marine X-band radar-image sequences. IEEE J. Ocean. Eng. 30 (3), 534–542. https://doi.org/10.1109/JOE.2005.857524.

Derkani, M.H., Alberello, A., Nelli, F., Bennetts, L.G., Hessner, K.G., MacHutchon, K., et al., 2021. Wind, waves, and surface currents in the Southern Ocean: observations from the Antarctic Circumnavigation Expedition. Earth Syst. Sci. Data 13, 1189–1209. https://doi.org/10.5194/essd-13-1189-2021.

Dodet, G., Piolle, J.-F., Quilfen, Y., Abdalla, S., Accensi, M., Ardhuin, F., et al., 2020. The Sea State CCI dataset v1: towards a sea state climate data record based on satellite observations. Earth Syst. Sci. Data 12, 1929–1951. https://doi.org/10.5194/essd-12-1929-2020.

Dodet, G., Abdalla, S., Alday, M., Accensi, M., Bidlot, J., Ardhuin, F., 2022. Error characterization of significant wave heights in multidecadal satellite altimeter product, model hindcast, and in situ measurements using the triple collocation technique. J. Atmos. Oceanic Technol. 39, 887–901. https://doi.org/10.1175/JTECH-D-21-0179.1.

Dodet, G., Mureau, G., Accensi, M., Piollé, J.F., 2025. Impact of altimeter-buoy data-pairing methods on the validation of Sentinel-3A coastal significant wave heights. Remote Sens. Environ. 316, 114483. https://doi.org/10.1016/j.rse.2024.114483.

Donelan, M.A., Curcic, M., Chen, I.S.S., Magnusson, A.K., 2012. Modeling waves and wind stress. J. Geophys. Res. Oceans 117, C11. https://doi.org/10.1029/2012JC007920.

Dremlyug, V.A., 1961. On the determination of some elements of sea waves using radar. Trans. AARI 210, 135–138 [in Russian].

Echevarria, E.R., Hemer, M.A., Holbrook, N.J., 2019. Seasonal variability of the global spectral wind wave climate. J. Geophys. Res. Oceans 124, 2924–2939. https://doi.org/10.1029/2018JC014620.

Erikson, L., Morim, J., Hemer, M., Young, I., Wang, X.L., Mentaschi, L., et al., 2022. Global ocean wave fields show consistent regional trends between 1980 and 2014 in a multi-product ensemble. Comm. Earth Environ. 3 (1), 320. https://doi.org/10.1038/s43247-022-00654-9.

Ermoshkin, A.V., Molkov, A.A., Kapustin, I.A., 2019. Statistical characteristics of Doppler velocity shift in artificial slick on sea surface. Remote Sens. 11150, 351–357. https://doi.org/10.1117/12.2533167, 2019.

Ermoshkin, A., Molkov, A., 2022. High-resolution radar sensing sea surface states during AMK-82 cruise. J. Sel. Top. Appl. Earth Obs. Remote Sens. 15, 2660–2666. https://doi.org/10.1109/JSTARS.2022.3161119.

Ermoshkin, A.V., Bogatov, N.A., Kapustin, I.A., Molkov, A.A., 2024. Determination of the significant wave height from Doppler radar images of the sea surface. Oceanology 64 (Suppl. 1), S29–S37. https://doi.org/10.1134/S000143702470084X.

Ezhova, E.A., Gavrikov, A.V., Sharmar, V.D., Tilinina, N.D., Suslov, A.I., Koshkina, V.S., et al., 2023. Obtaining wind wave parameters using ship radar. Oceanology 63 (Suppl. 1), S42–S53. https://doi.org/10.1134/S0001437023070032.

Ezhova, E.A., Gavrikov, A.V., Tilinina, N.D., 2024. The validity domain of satellite altimetry data for validation of algorithms for estimation wind wave height. J. Oceanol. Res. 52 (4), 39. https://doi.org/10.29006/1564-2291.JOR-2024.52(4).3 [in Russian].

Ezhova, E., Gavrikov, A., Sharmar, V., Gladyshev, V., Suslov, A., Koshkina, V., et al., 2025. Shipborne X-band radar observations of ocean wind waves during IO RAS expeditions with SeaVision. PANGAEA. https://doi.org/10.1594/PANGAEA.983956 (dataset in review). [Dataset].

FAO, 2024. The state of world fisheries and aquaculture 2024. https://openknowledge.fao.org/server/api/core/bitstreams/66538eba-9c85-4504-8438-c1cf0a0a3903/content/sofia/2024/fishing-fleet.html accessed 22 March 2025.

Freeman, E., et al., 2017. ICOADS Release 3.0: a major update to the historical marine climate record. Int. J. Climatol. 37, 2211–2232. https://doi.org/10.1002/joc.4775.

Gavrikov, A., Ivonin, D., Sharmar, V., Tilinina, N., Gulev, S., Suslov, A., et al., 2021. Wind waves in the North Atlantic and Arctic from ship navigational radar (SeaVision system) and wave buoy Spotter during three research cruises in 2020 and 2021. PANGAEA. https://doi.org/10.1594/PANGAEA.939620 [Dataset].

Greenwood, C., Vogler, A., Morrison, J., Murray, A., 2018. The approximation of a sea surface using a shore-mounted X-band radar with low grazing angle. Remote Sens. Environ. 204, 439–447. https://doi.org/10.1016/j.rse.2017.10.012.

Grigorieva, V.G., Badulin, S.I., Gulev, S.K., 2022. Global validation of SWIM/CFOSAT wind waves against voluntary observing ship data. Earth Space Sci. 9, e2021EA002008. https://doi.org/10.1029/2021EA002008.

Gulev, S.K., Hasse, L., 1998. North Atlantic wind waves and wind stress fields from voluntary observing ship data. J. Phys. Oceanogr. 28, 1107–1130. https://doi.org/10.1175/1520-0485(1998)028%3C1107:NAWWAW%3E2.0.CO;2.

Gulev, S.K., Grigorieva, V., Sterl, A., Woolf, D., 2003. Assessment of the reliability of wave observations from voluntary observing ships: insights from the validation of a global wind wave climatology based on voluntary observing ship data. J. Geophys. Res. Oceans 108. https://doi.org/10.1029/2002JC001437.

Gulev, S.K., Grigorieva, V., 2004. Last century changes in ocean wind wave height from global visual wave data. Geophys. Res. Lett. 31. https://doi.org/10.1029/2004GL021040.

Gulev, S.K., Grigorieva, V., 2006. Variability of the winter wind waves and swell in the North Atlantic and North Pacific as revealed by the voluntary observing ship data. J. Climate 19, 5667–5685. https://doi.org/10.1175/JCLI3936.1.

Gulev, S., Jung, T., Ruprecht, E., 2007. Estimation of the impact of sampling errors in the VOS observations on air–sea fluxes. Part I: uncertainties in climate means. J. Climate 20, 279–301. https://doi.org/10.1175/JCLI4010.1.

Hessner, K., Hanson, J.L., 2010. Extraction of coastal wavefield properties from X-band radar. In: 2010 IEEE Int. Geosci. Remote Sens. Symp. Honolulu, HI, USA, pp. 4326–4329. https://doi.org/10.1109/IGARSS.2010.5650134.

Hessner, K.G., El Naggar, S., von Appen, W.-J., Strass, V.H., 2019. On the reliability of surface current measurements by X-band marine radar. Remote Sens. 11, 1030. https://doi.org/10.3390/rs11091030.

Horstmann, J., Nieto Borge, J.C., Seemann, J., Carrasco, R., Lund, B., 2015. Wind, wave, and current retrieval utilizing X-band marine radars. Coastal Ocean Observ. Syst. 16, 281–304. https://doi.org/10.1016/B978-0-12-802022-7.00016-X. Amsterdam, The Netherlands: Elseiver.

Horstmann, J., Bödewadt, J., Carrasco, R., Cysewski, M., Seemann, J., Streßer, M., 2021. A coherent on-receive X-band marine radar for ocean observations. Sensors 21 (23), 7828. https://doi.org/10.3390/s21237828.

Huang, W., Liu, X., Gill, E.W., 2017. Ocean wind and wave measurements using X-band marine radar: a comprehensive review. Remote Sens. 9. https://doi.org/10.3390/rs9121261.

Hwang, P.A., Sletten, M.A., Toporkov, J.V., 2010. A note on Doppler processing of coherent radar backscatter from the water surface: with application to ocean surface wave measurements. J. Geophys. Res. 115, C03026. https://doi.org/10.1029/2009JC005870.

Ijima, T., Takahashi, T., 1964. Application of radar to wave direction observation etc. In: Proc. 11th Japanese Conf. Coast. Eng, pp. 81–88.

Jiang, H., Mu, L., 2019. Wave climate from spectra and its connections with local and remote wind climate. J. Phys. Oceanogr. 49, 543–559. https://doi.org/10.1175/JPO-D-18-0149.1.

Jiang, H., 2020. Wave climate patterns from spatial tracking of global long-term ocean wave spectra. J. Climate 33, 3381–3393. https://doi.org/10.1175/JCLI-D-19-0729.1.

Kent, E.C., Rayner, N.A., Berry, D.I., Eastman, R., Grigorieva, V.G., Huang, B., et al., 2019. Observing requirements for long-term climate records at the ocean surface. Front. Mar. Sci. 6, 441. https://doi.org/10.3389/fmars.2019.00441.

Kodaira, T., Nose, S., Sato, K., Ohshima, K.I., Noda, H., Ushio, S., Ryu, J., 2021. Observation of on-ice wind waves under grease ice in the western Arctic Ocean. Polar Sci. 27, 100567. https://doi.org/10.1016/j.polar.2020.100567.

Kozlov, I.E., Kopyshov, I.O., Frey, D.I., Morozov, E.G., Medvedev, I.P., Shiryborova, A.I., et al., 2023. Multi-sensor observations reveal large-amplitude nonlinear internal waves in the Kara Gates, Arctic Ocean. Remote Sens. 15, 5769. https://doi.org/10.3390/rs15245769.

Mahrt, L., Nilsson, E., Rutgersson, A., 2022. The sea surface heat flux at a coastal site. J. Phys. Oceanogr. 52, 3297–3307. https://doi.org/10.1175/JPO-D-22-0094.1.

Makin, V.K., Mastenbroek, C., 1996. Impact of waves on air–sea exchange of sensible heat and momentum. Boundary-Layer Meteorol. 79, 279–300. https://doi.org/10.1007/bf00119442.

Li, B., Xu, J., Pan, X., Ma, L., Zhao, Z., Chen, R., Liu, Q., Wang, H., 2022. Marine oil spill detection with X-band shipborne radar using GLCM, SVM, and FCM. Remote Sens. 14, 3715. https://doi.org/10.3390/rs14153715.

Liu, Q., Babanin, A.V., Zieger, S., Young, I.R., Guan, C., 2016. Wind and wave climate in the Arctic Ocean as observed by altimeters. J. Clim. 29, 7957–7975. https://doi.org/10.1175/JCLI-D-16-0219.1.

Liu, C., Freemann, E., Kent, E.C., Berry, D.I., Worley, S.J., Smith, S.R., et al., 2022. Blending TAC and BUFR marine in situ data for ICOADS near-real-time release 3.0.2. J. Atmos. Oceanic Technol. 39, 1943–1959. https://doi.org/10.1175/JTECH-D-21-0182.1.

Liu, Y., Wang, X., Yang, Q., Liu, F., Zhang, J., 2023. Rainfall detection in marine radar data based on image processing and deep learning. Energy Rep. 9, 5632–5641. https://doi.org/10.1016/j.egyr.2023.04.287.

Liu, B., Liu, K., Li, C., 2024. Advanced analysis of marine structures. J. Mar. Sci. Eng. 12, 1111. https://doi.org/10.3390/jmse12071111.

Lobeto, H., Menendez, M., Losada, I.J., Hemer, M., 2022. The effect of climate change on wind-wave directional spectra. Global Planet. Change 213, 103820. https://doi.org/10.1016/j.gloplacha.2022.103820.

Lund, B., Graber, H.C., Romeiser, R., 2012. Wind retrieval from shipborne nautical X-band radar data. IEEE Trans. Geosci. Remote Sens. 50, 3800–3811. https://doi.org/10.1109/TGRS.2012.2186457.

Lund, B., Graber, H.C., Xue, J., Romeiser, R., 2013. Analysis of internal wave signatures in marine radar data. IEEE Trans. Geosci. Remote Sens. 51, 4840–4852. https://doi.org/10.1109/TGRS.2012.2230635.

Lund, B., Collins III, C.O., Graber, H., Terrill, E., Herbers, T., 2014. Marine radar ocean wave retrieval's dependency on range and azimuth. Ocean Dyn. 64, 1–20. https://doi.org/10.1007/s10236-014-0725-6.

Lund, B., Graber, H.C., Tamura, H., Collins III, C.O., Varlamov, S.M., 2015. A new technique for the retrieval of near-surface vertical current shear from marine X-band radar images. J. Geophys. Res. Oceans 120, 8466–8486. https://doi.org/10.1002/2015JC010961.

Lund, B., Graber, H.C., Persson, P.O.G., Smith, M., Doble, M., Thomson, J., Wadhams, P., 2018a. Arctic sea ice drift measured by shipboard marine radar. J. Geophys. Res. Oceans 123, 4298–4321. https://doi.org/10.1029/2018JC013769.

Lund, B., Haus, B., Horstmann, J., Graber, H.C., Carrasco, R., Laxague, N.J.M., Novelli, G., Guigand, C.M., Ozgokmen, T.M., 2018b. Near-surface current mapping by shipboard marine X-band radar: a validation. J. Atmos. Oceanic Technol. 35 (5), 1077–1090. https://doi.org/10.1175/JTECH-D-17-0154.1.

Magnusson, A.K., Jensen, R., Swail, V., 2021. Spectral shapes and parameters from three different wave sensors. Ocean Dyn. 71, 893–909. https://doi.org/10.1007/s10236-021-01468-7.

Nieto Borge, J.C., Reichert, K., Dittmer, J., 1999. Use of nautical radar as a wave monitoring instrument. Coast. Eng. 37, 331–342. https://doi.org/10.1016/S0378-3839(99)00032-0.

Nieto Borge, J.C., Guedes Soares, C., 2000. Analysis of directional wave fields using X-band navigation radar. Coast. Eng. 40 (4), 375–391. https://doi.org/10.1016/S0378-3839(00)00019-3.

Nieto Borge, J.C., Rodríguez, G.R., Hessner, K., González, P.I., 2004. Inversion of marine radar images for surface wave analysis. J. Atmos. Oceanic Technol. 21, 1291–1300. https://doi.org/10.1175/1520-0426(2004)021<1291:IOMRIF>2.0.CO;2.

Nieto-Borge, J.C., Hessner, K., Jarabo-Amores, P., de la Mata-Moya, D., 2008. Signal-to-noise ratio analysis to estimate ocean wave heights from X-band marine radar image time series. IET Radar. Sonar. Navig. 2, 35–41. https://doi.org/10.1049/iet-rsn:20070027.

Peláez-Zapata, D., Pakrashi, V., Dias, F., 2024. Ocean wave directional distribution from GPS buoy observations off the west coast of Ireland: assessment of a wavelet-based method. J. Atmos. Oceanic Technol. 41, 749–765. https://doi.org/10.1175/JTECH-D-23-0058.1.

Raghukumar, K., Chang, G., Spada, F., Jones, C., Janssen, T., Gans, A., 2019. Performance characteristics of "Spotter," a newly developed real-time wave measurement buoy. J. Atmos. Oceanic Technol. 36, 1127–1141. https://doi.org/10.1175/JTECH-D-18-0151.1.

Reichert, K., Hessner, K., Nieto Borge, J.C., Dittmer, J., 1999. WaMoS-II: a radar-based wave and current monitoring system. In: Proc. 9th Int. Offshore Polar Eng. Conf. (ISOPE). Brest, France. May 1999, ID: ISOPE-I-99-246.

Seemann, J., Ziemer, F., Senet, C.M., 1997. A method for computing calibrated ocean wave spectra from measurements with a nautical X-band radar. Oceans '97. MTS/IEEE Conf. Proc 2, 1148–1154. https://doi.org/10.1109/OCEANS.1997.624154.

Sharmar, V.D., Markina, M.Y., Gulev, S.K., 2021. Global ocean wind-wave model hindcasts forced by different reanalyses: a comparative assessment. J. Geophys. Res. Oceans 126, e2020JC016710. https://doi.org/10.1029/2020JC016710.

Shin, M.S., Ki, M.S., Lee, G.J., Park, B.J., Lee, Y.Y., Kim, Y., Lee, S.B., 2020. Discussions on availability of weather information data and painting effect of existing 8600 TEU container ship using ship performance analysis program. J. Ocean Eng. Technol. 34, 377–386. https://doi.org/10.26748/KSOE.2020.057.

Smith, S.R., Alory, G., Andersson, A., Asher, W., Baker, A., Berry, D.I., et al., 2019. Ship-based contributions to global ocean, weather, and climate observing systems. Front. Mar. Sci. 6, 434. https://doi.org/10.3389/fmars.2019.00434.

Støle-Hentschel, S., Carrasco, R., Nieto-Borge, J.C., Seemann, J., Toledo, Y., 2024. Improved estimation of the directional wave spectrum from marine radar images by employing a directional modulation transfer function (MTF). Ocean Eng. 307, 118–126. https://doi.org/10.1016/j.oceaneng.2024.118126.

Sun, L., Lu, Z., Wang, Z., Liu, H., Shang, H., 2022. A wave texture difference method for rainfall detection using X-band marine radar. J. Electr. Electr. Eng. 1–14. https://doi.org/10.1155/2022/1068885.

Taburet, N., Husson, R., Charles, E., Jettou, G., Philip, A., Philipps, S., Ghantous, M., Kocha, C., 2023. Quality information document for WAVE Thematic Assembly Centre product WAVE_GLO_PHY_SWH_L3_NRT_014_001. https://doi.org/10.48670/moi-00179.

Tilinina, N., Ivonin, D., Gavrikov, A., Sharmar, V., Gulev, S., Suslov, A., et al., 2022. Wind waves in the North Atlantic from ship navigational radar: seaVision development and its validation with spotter wave buoy and WaveWatch III. Earth Syst. Sci. Data 14, 3615–3639. https://doi.org/10.5194/essd-14-3615-2022.

UNCTAD, 2024. Vessel value by ownership. https://unctadstat.unctad.org/datacentre/dataviewer/US.VesselValueByOwnership accessed 22 March 2025.

Villas Boas, A.B., Ardhuin, F., Ayet, A., Bourassa, M.A., Brandt, P., Chapron, B., et al., 2019. Integrated observations of global surface winds, currents, and waves: requirements and challenges for the next decade. Front. Mar. Sci. 6, 425. https://doi.org/10.3389/fmars.2019.00425.

Vicen-Bueno, R., Horstmann, J., Terril, E., de Paolo, T., Dannenberg, J., 2013. Real-time ocean wind vector retrieval from marine radar image sequences acquired at grazing angle. J. Atmos. Oceanic Technol. 30, 127–139. https://doi.org/10.1175/JTECH-D-12-00027.1.

Westbrook, E., Gaube, P., Culhane, E., Bingham, F., Pacini, A., Schmidgall, C., Schanze, J., and Drushka, K., 2025: Classification of sea-ice concentration from ship-board S-band radar images using open-source machine learning tools, EGUsphere [preprint], https://doi.org/10.5194/egusphere-2025-643.

WMO, 2023. Manual on the Global Telecommunication System. Annex III to the WMO Technical Regulations. WMO-No. 386, Geneva. https://library.wmo.int/viewer/35800/download?file=386_2023-edition_en.pdf&type=pdf&navigator=1.

Wu, L., Sahlée, E., Nilsson, E., Rutgersson, A., 2024. A review of surface swell waves and their role in air–sea interactions. Ocean Modell. 190, 102397. https://doi.org/10.1016/j.ocemod.2024.102397.

Yang, Z., Huang, W., Chen, X., 2021. Evaluation and mitigation of rain effect on wave direction and period estimation from X-band marine radar images. IEEE J. Selected Topics Appl. Earth Observ. Remote Sens. 14, 5207–5219. https://doi.org/10.1109/JSTARS.2021.3076693.

Young, I.R., Rosenthal, W., Ziemer, F., 1985. A three-dimensional analysis of marine radar images for the determination of ocean wave directionality and surface currents. J. Geophys. Res. Oceans 90, 1049–1059. https://doi.org/10.1029/JC090iC01p01049.

Ziemer, F., Dittmer, J., 1994. A system to monitor ocean wave fields. In: Proc. OCEANS'94, Brest, France 2, II/28–II/31. https://doi.org/10.1109/OCEANS.1994.364010.

Zemp, M. 2022. GCOS 2022 Implementation Plan. In: Chao, Qingchen; Han Dolman, Albertus Johannes; Herold, Martin; Krug, Thelma; Speich, Sabrina; Suda, Kazuto; Thorne, Peter; Yu, Weidong; Zemp, Michael. The 2022 GCOS Implementation Plan. Geneva: World Meteorological Organization, 85. https://gcos.wmo.int/site/global-climate-observing-system-gcos/essential-climate-variables/sea-state.